

1 **Holocene climates of the Iberian Peninsula: pollen-based reconstructions of changes in**
2 **the west-east gradient of temperature and moisture**

3 Mengmeng Liu^{1,*}, Yicheng Shen², Penelope González-Sampéris³, Graciela Gil-Romera³,
4 Cajo J. F. ter Braak⁴, Iain Colin Prentice¹, Sandy P. Harrison²

5 1: Department of Life Sciences, Imperial College London, Silwood Park Campus, Buckhurst
6 Road, Ascot SL5 7PY, UK

7 2: Geography & Environmental Science, Reading University, Whiteknights, Reading, RG6
8 6AH, UK

9 3: Instituto Pirenaico de Ecología-CSIC, Avda. Montañana 1005, 50059, Zaragoza, Spain

10 4: Biometris (Applied Mathematics and Applied Statistics Centre), Wageningen University &
11 Research, 6708 PB Wageningen, The Netherlands

12 *: Corresponding author: Mengmeng Liu (m.liu18@imperial.ac.uk)

13 Ms for: *Climate of the Past*

14 **Abstract**

15 The Iberian Peninsula is characterised by a steep west-east moisture gradient today, reflecting
16 the dominance of maritime influences along the Atlantic coast and more Mediterranean-type
17 climate further east. Holocene pollen records from the Peninsula suggest that this gradient was
18 less steep during the mid-Holocene, possibly reflecting the impact of orbital changes on
19 circulation and thus regional patterns in climate. Here we use 7214 pollen samples from 117
20 sites covering part or all of the last 12,000 years to reconstruct changes in seasonal temperature
21 and in moisture across the Iberian Peninsula quantitatively. We show that there is an increasing
22 trend in winter temperature at a regional scale, consistent with known changes in winter
23 insolation. However, summer temperatures do not show the decreasing trend through the
24 Holocene that would be expected if they were a direct response to insolation forcing. We show
25 that summer temperature is strongly correlated with plant-available moisture (α), as measured
26 by the ratio of actual evapotranspiration to equilibrium evapotranspiration, which declines
27 through the Holocene. The reconstructions also confirm that the west-east gradient in moisture
28 was considerably less steep than today during the mid-Holocene, indicating that atmospheric
29 circulation changes (possibly driven by orbital changes) have been important determinants of
30 the Holocene climate of the region.

31 1. Introduction

32 The Iberian Peninsula is characterised by a steep west-east gradient in temperature and
33 moisture today, reflecting the dominance of maritime influences along the Atlantic coast and
34 more Mediterranean-type climate further east. Projections of future climate change suggest that
35 the region will become both warmer and drier, but nevertheless show that this west-east
36 differentiation is maintained (Andrade et al., 2021a). The changes in temperature are projected
37 to be larger and the occurrence of extreme temperature episodes more frequent in the south-
38 central and eastern parts of Iberia than in Atlantic coastal areas (Carvalho et al., 2021). Similar
39 gradients are seen in future projections of precipitation change, with largest reductions in
40 precipitation in the south-central region (Andrade et al., 2021b). However, the stability of these
41 west-east gradients during the Holocene has been questioned. In particular, the west-east
42 gradient in moisture appears to have been less pronounced during the mid-Holocene (8–4
43 ka) when cooler summers and wetter conditions in the Atlantic zone (e.g. Martínez-Cortizas et
44 al., 2009; Mauri et al., 2015) coincided with the maximum development of mesophytic
45 vegetation further east and south (Aranbarri et al., 2014, 2015; Carrión et al., 2010, 2009;
46 González-Sampériz et al., 2017).

47 However, much of the evidence for Holocene climates of the Iberian Peninsula is based on
48 qualitative interpretations of vegetation changes, generally interpreted as reflecting changes in
49 moisture availability (Morellón et al., 2018; Ramos-Román et al., 2018; Schröder et al., 2019).
50 These records are extensive and they seem to indicate fairly complex spatial patterns of change.
51 Kaufman et al. (2020) provides quantitative reconstructions of summer and winter temperature
52 in their compilation of Holocene climate information, but there are only 5 terrestrial sites from
53 the Iberian Peninsula. Iberia was also included in the quantitative pollen-based reconstructions
54 of European climate through the Holocene in (Mauri et al., 2015), which is an update of (Davis
55 et al., 2003). However, the geographical distribution of sites included is uneven and a large
56 fraction of the records were from the Pyrenees and the Cantabrian mountains, with additional
57 clustering of sites in coastal regions. Thus, the inferred patterns of climate over most of the
58 central part of the Peninsula are therefore largely extrapolated. Tarroso et al. (2016) has
59 provided reconstructions of summer and winter temperature and mean annual precipitation
60 since the Last Glacial Maximum for the Iberian Peninsula, by using modern species distribution
61 data to develop climate probability distribution functions (PDFs) and applying these to 31 fossil
62 records. However, although they identified trends in precipitation during the Holocene, the

63 temperature reconstructions do not seem to be reliable since they show no changes through
64 time (9~3 ka), either for the Iberian Peninsula as a whole or for individual sub-regions, in
65 ~~contradiction~~ ~~contra-distinction~~ to the other reconstructions. The current state of uncertainty
66 about Holocene climate changes in Iberia is further exacerbated because quantitative
67 reconstructions of summer temperature made at individual sites using chironomid data (Muñoz
68 Sobrino et al., 2013; Tarrats et al., 2018) are not consistent with reconstructed summer
69 temperatures based on pollen for the same sites.

70 Here, using pollen-inferred transfer functions, ~~Here~~ we re-examine the trends in summer and
71 winter temperature and plant-available moisture through the Holocene across Iberia, using a
72 new and relatively comprehensive compilation of pollen data (Shen et al., 2022) with age
73 models based on the latest radiocarbon calibration curve (IntCal20: Reimer et al., 2020). We
74 explicitly test whether there are significant differences in the west-east gradient of moisture
75 and temperature through time. We then analyse the relationships between the changes in the
76 three climate variables and how trends in these variables are related to external climate forcing.
77 These analyses allow us to ~~confirm~~ investigate whether ~~that~~ the west-east gradient in moisture
78 was less steep during the mid-Holocene and explore what controls the ~~and indicate the~~
79 ~~importance of changes in atmospheric circulation in explaining observed~~ patterns of climate
80 change across the region.

81 **2. Methods**

82 Multiple techniques have been developed to make quantitative climate reconstructions from
83 pollen (see reviews in Bartlein et al., 2011; Chevalier et al., 2020; Salonen et al., 2011). Modern
84 analogue techniques (MAT: Overpeck et al., 1985) tend to produce rapid shifts in reconstructed
85 values corresponding to changes in the selection of the specific analogue samples, although
86 this tendency is less marked in the conceptually analogous response surface technique (Bartlein
87 et al., 1986). Regression-based techniques, including weighted averaging methods such as
88 Weighted Average Partial Least-Squares (WAPLS: ter Braak and Juggins, 1993), do not
89 produce step-changes in the reconstructions but suffer from the tendency to compress the
90 reconstructions towards the central part of the sampled climate range. However, this tendency
91 can be substantially reduced by accounting for the sampling frequency (f_x) and the climate
92 tolerance of the pollen taxa present in the training data set (f_x TWA-PLS: Liu et al., 2020).
93 Machine-learning and Bayesian approaches have also been applied to derive climate
94 reconstructions from pollen assemblages (Peyron et al., 1998; Salonen et al., 2019). However,

95 comparison of fxTWA-PLS with the Bayesian model BUMPER (Holden et al., 2017), shows
96 that fxTWA-PLS performs better in capturing the climate of the modern training data set from
97 Europe (Liu et al., 2020).

98 Although fxTWA-PLS has clear advantages over other quantitative reconstructions techniques,
99 there is still a slight tendency towards compression. We have therefore made a further
100 modification to the approach as described in Liu et al. (2020). In the original version of
101 fxTWA-PLS, the fx correction is applied as a weight with the form of $1/fx^2$ in the regression
102 (step 7 in Table 1 in Liu et al., 2020). Here (see Appendix A) we make a further modification
103 of fxTWA-PLS by (a) applying the fx correction separately in both the taxon calculation and
104 the regression (step 2 and 7 in Table 1 in Liu et al., 2020) as a weight with the form of $1/fx$ and
105 (b) applying P-splines smoothing (Eilers and Marx, 2021) in order to reduce the dependence
106 of the fx estimation on bin width. The modified version further reduces the biases at the
107 extremes of the sampled climate range. We used this modified version of fxTWA-PLS to
108 reconstruct three climate variables: mean temperature of the coldest month (MTCO), mean
109 temperature of the warmest month (MTWA) and plant-available moisture represented by α , an
110 estimate of the ratio of actual evapotranspiration to equilibrium evapotranspiration. The
111 individual and joint effects of MTCO, MTWA and α were tested explicitly using canonical
112 correspondence analysis (CCA). The modified version further reduces the biases at the
113 extremes of the sampled climate range, while retaining the desirable properties of WA-PLS in
114 terms of robustness to spatial autocorrelation (fxTWA-PLS: Liu et al., 2020).

115 The modern pollen training dataset was derived from the SPECIAL Modern Pollen Data Set
116 (SMPDS: Harrison, 2019). The SMPDS consists of relative abundance records from 6458
117 terrestrial sites from Europe, northern Africa, the Middle East and northern Eurasia (SI Figure
118 S1) assembled from multiple different published sources. The pollen records were
119 taxonomically standardized, and filtered (as recommended by Chevalier et al., 2020) to remove
120 obligate aquatics, insectivorous species, introduced species, and taxa that only occur in
121 cultivation (see SI Table S1 for the list). Taxa (mainly herbaceous) with only sporadic
122 occurrences were amalgamated to higher taxonomic levels (genus, sub-family or family) after
123 ensuring consistency with their distribution in climate space. As a result of these
124 amalgamations, the SMPDS contains data on 247 pollen taxa. For our analysis, we use the 195
125 taxa that occur at more than 10 sites.

126 Modern climate data at each of the sites in the training data set were obtained from Harrison

127 (2019). This data set contains climate reconstructions of MTCO, growing degree days above a
 128 baseline of 0°C (GDD_0) and a moisture index (MI), defined as the ratio of annual precipitation
 129 to annual potential evapotranspiration. The climate at each site was obtained using
 130 geographically-weighted regression of the CRU CL v2.0 gridded dataset of modern (1961-
 131 1990) surface climate at 10 arc minute resolution (New et al., 2002) in order to correct for
 132 elevation differences between each pollen site and the corresponding grid cell. The
 133 geographically-weighted regression used a fixed bandwidth kernel of 1.06° ($\sim 140\text{km}$) to
 134 optimize model diagnostics and reduce spatial clustering of residuals relative to other
 135 bandwidths. The climate of each pollen site was then estimated based on its longitude, latitude,
 136 and elevation. MTCO and GDD_0 was taken directly from the GWR regression and MI was
 137 calculated for each pollen site using a modified code from SPLASH v1.0~~MI was calculated for~~
 138 ~~each pollen site using code modified from SPLASH v1.0~~ (Davis et al., 2017) based on daily
 139 values of precipitation, temperature and sunshine hours again obtained using a mean-
 140 conserving interpolation of the monthly values of each. For this application, we used MTCO
 141 directly from the data set but calculated MTWA from MTCO and GDD_0 , based on the
 142 relationship between MTCO, MTWA and GDD_0 given by Appendix 2 of Wei et al. (2021).
 143 We derived α from MI following Liu et al. (2020). The modern training data set provides
 144 records spanning a range of MTCO from -42.4°C to 14.8°C , of MTWA from 4.2°C to 33.5
 145 $^{\circ}\text{C}$, and of α from 0.04 to 1.25 (Figure-Fig. 1, SI Fig. S1).

146 The fossil pollen data from the Iberian Peninsula were compiled by Shen et al. (2021) and the
 147 data set was obtained from ~~(Harrison et al. (-2022))~~~~(Harrison et al., 2022) was obtained from~~
 148 <https://doi.org/10.17864/1947.000369>. The taxonomy used by Shen et al. (2021) is consistent
 149 with that employed in the SMPDS. Shen et al. (2021) provides consistent age models for all
 150 the records based on the IntCal20 calibration curve (Reimer et al., 2020) and the BACON
 151 Bayesian age-modelling tool (Blaauw et al., 2021; Blaauw and Christeny, 2011) using the
 152 supervised modelling approach implemented in the `ageR` package (Villegas-Diaz et al, 2021).
 153 We excluded individual pollen samples with large uncertainties (standard error larger than 100
 154 years) on the attributed in the new age model. As a result, the climate reconstructions are based
 155 on a fossil data set of 7384 pollen samples from 117 records covering part or all of the last
 156 12,000 years (Figure-Fig. 2), with 42 individual records provided by the original authors, 73
 157 records obtained from the European Pollen Database (EPD, www.europeanpollendatabase.net)
 158 and 2 records from PANGAEA (www.pangaea.de/). Details of the records are given in ~~SI~~Table
 159 **S1**. The average temporal resolution of these records is 101 years. We then excluded a few

160 samples where the reconstructed values of α exceed the natural limit of 0 and 1.26. Finally,
161 7214 samples from 117 records are used for the analyses of the climate reconstructions.
162 Summer insolation and winter insolation are also calculated using the PAST software based on
163 the age and latitude of each sample (Hammer et al., 2001).

164 Variance inflation factor (VIF) scores are calculated for both the modern climates and the
165 climates reconstructed from fossil pollen records, in order to avoid multicollinearity problems
166 and thus guarantee the climate variables (MTCO, MTWA, α) used here represent independent
167 features of the pollen records.

168

169 In addition to examining the reconstructions for individual sites, we constructed composite
170 curves for the Iberian Peninsula as a whole. The composite curves provide a way of comparing
171 the relationship between trends in the reconstructed climate changes and insolation changes.
172 The curves were constructed after binning the site-based reconstructions using ± 500 -year bins.
173 We did 1000 bootstrap resampling of the reconstructed climate values in each ± 500 -year bin
174 to avoid the influence of a single value or a single site on the mean climate value in this bin,
175 and use the standard deviation of the 1000 values to represent the uncertainty of the mean
176 climate value. We constructed linear regression plots to examine the longitudinal and
177 elevational patterns in the reconstructed climate variables, and assessed the significance of
178 differences in these trends through time compared to the most recent bin ($0.5 \text{ ka} \pm 500 \text{ years}$)
179 based on p values, with the customary threshold of 0.05. We then compared the climate trends
180 with changes in summer and winter insolation.

181 3. Results

182 The modified version of fxTWA-PLS reproduces the modern climate reasonably well (~~Table~~
183 ~~4~~Table 2). The performance is best for MTCO (R^2 0.75, RMSEP 4.70, slope 0.91) but is also
184 good for α (R^2 0.68, RMSEP 0.16, slope 0.78) and MTWA (R^2 0.57, RMSEP 3.47, slope 0.71).
185 The correlations between pollen records and each of the three bioclimate variables, as assessed
186 by CCA, were strong for both modern climate data and fossil reconstructions (~~Table 2~~Table 3).
187 The variance inflation factor (VIF) scores are all less than 6, so there are no multicollinearity
188 problems (~~Table 2~~Table 3) (Allison, 1994). Furthermore, the taxa that contribute most strongly
189 to reconstructing colder/warmer or wetter/drier climates show predictable patterns consistent
190 with their known ecological preferences (SI ~~Table S~~Table S22).

191 Winters were generally colder than present during the early to mid-Holocene, as shown by the
192 coherent patterns of reconstructed anomalies at individual sites (Fig. 3a, 3d). Here “present”
193 means the most recent pollen bin ($0.5 \text{ ka} \pm 500 \text{ years}$). The composite curve also shows a
194 general increase in winter temperatures through time (Fig. 4a), consistent with the trend in
195 winter insolation (Fig. 4d). The composite curve shows that it was ca 4°C cooler than today at
196 11.5 ka and conditions remained cooler than present until ca 2.5 ka. Winter temperatures today
197 increase from north to south and are also affected by elevation; these patterns are still present
198 in the Holocene reconstructions, but there is no spatial differentiation between western and
199 eastern Iberia in the anomalies ~~Winter temperature anomalies show no spatial differentiation~~
200 ~~between western and eastern Iberia~~ (Table 3 Table 4, SI Fig. S2). The similarity of the changes
201 compared to present geographically is consistent with the idea that the changes in winter
202 temperature are driven by changes in winter insolation.

203 Summers were somewhat hotter than present in the west and cooler than present in the east
204 during the early and mid-~~dle~~-Holocene, as shown by the reconstructed anomalies at individual
205 sites (Fig. 3b, 3e). This west-east difference could not arise if the changes in summer
206 temperatures were a direct reflection of the insolation forcing (Fig. 4e). Indeed, the composite
207 curve shows relatively little change in MTWA (Fig. 4b), confirming that there is no direct
208 relationship to insolation forcing (Fig. 4e).

209 There is a strong west-east gradient in α at the present day (Fig. 2), with wetter conditions in
210 the west and drier conditions in the east. However, the reconstructed anomalies at individual
211 sites (Fig. 3c, 3f) suggest that west was drier and the east was wetter than present in the mid-
212 Holocene, resulting in a flatter west-east gradient. The west-east gradient is significantly
213 different from present between 9.5 ~ 3.5 ka (Fig. 5, ~~Table 3~~ Table 4), implying stronger
214 moisture advection into the continental interior during the mid-Holocene. The change in
215 gradient is seen in both high and low elevation sites (SI Fig. S3). There is also significant
216 change in α with elevation between 9.5 ~ 4.5 ka (~~Table 3~~ Table 4, SI Fig. S4).

217 Summer temperatures are strongly correlated with changes in α , both in terms of spatial
218 correlations in the modern data set at a European scale and in terms of spatial and temporal
219 correlations the fossil data set from Iberian Peninsula (Fig. 6). The patterns of reconstructed
220 anomalies in MTWA and α at individual sites are also coherent (Fig. 3b, 3c, 3e, 3f), showing
221 drier conditions and hotter summers than present in the west and wetter conditions with cooler
222 summers in the east during the early to mid-Holocene. The west-east gradient in MTWA was

223 significantly different from present between 9.5 and 3.5 ka except 8.5 ka (~~Table 3~~Table 4, SI
224 Fig. S5), roughly the interval when the gradient in α was also significantly different from
225 present. Again, the change in the east-west gradient is registered at both high and low elevation
226 sites (SI Fig. S6). However, there is no significant change in MTWA with elevation except 8.5
227 and 7.5 ka (~~Table 3~~Table 4, SI Fig. S7).

228 4. Discussion

229 We have shown that there was a gradual increase in MTCO over the Holocene, both for most
230 of the individual sites represented in the data set and for Iberia as a whole. Colder winters in
231 southern Europe during the mid-Holocene (6 ka) are a feature of many earlier reconstructions
232 (e.g. Cheddadi et al., 1997; Wu et al., 2007). A general warming trend over the Holocene is
233 seen in gridded reconstructions of winter season (December, January, February) temperatures
234 as reconstructed using the modern analogue approach by Mauri et al. (2015), although there is
235 somewhat less millennial-scale variability in these reconstructions (~~SI Fig. S8~~Fig. 7).
236 Nevertheless, their reconstructions show a cooling of 3°C in the early Holocene, comparable
237 in magnitude to the ca 4°C cooling at 11.5 ka reconstructed here. Although they show
238 conditions slightly cooler than present persisting up to 1 ka, the differences are very small (ca
239 0.5°C) after 2 ka, again consistent with our reconstructions of MTCO similar to present by 2.5
240 ka. Quantitative reconstructions of winter temperature for the 5 terrestrial sites from the Iberian
241 Peninsula in the Kaufman et al. (2020) compilation all show a general trend of winter warming
242 over the Holocene, but the magnitude of the change at some of the individual sites is much
243 larger (ca 10°C) and there is no assessment of the uncertainty on these reconstructions. The
244 composite curve of Kaufman et al. (2020) shows an increasing trend in MTCO through the
245 Holocene although with large uncertainties (~~SI Fig. S8~~Fig. 7). In contrast to the consistency of
246 the increasing trend in MTCO during the Holocene between our reconstructions and those of
247 Mauri et al. (2015) and Kaufman et al. (2020), there is no discernible trend in MTCO during
248 the Holocene reconstruction of Tarroso et al. (2016). Indeed, there is no significant change in
249 their MTCO values after ca 9 ka, either for the Peninsula as a whole (~~SI Fig. S8~~Fig. 7) or for
250 any of the four sub-regions they considered. Our reconstructed trend in winter temperature is
251 consistent with the changes in insolation forcing at this latitude during the Holocene, and is
252 also consistent with transient climate model simulations (Braconnot et al., 2019; Carré et al.,
253 2021; Dallmeyer et al., 2020; Parker et al., 2021) of the winter temperature response to
254 changing insolation forcing over the late Holocene in this region (~~SI Fig. S9~~Fig. 8, SI Fig. S8).

255 Thus, we suggest that changes in winter temperatures are a direct consequence of insolation
256 forcing.

257 We have shown that there is no overall trend in MTWA during the Holocene. According to our
258 reconstructions, summer temperatures fluctuated between ca 0.5°C above or below modern
259 temperature. The lack of coherent trend in MTWA is consistent with the gridded
260 reconstructions of summer (June, July, August) temperature in the Mauri et al. (2015) data set
261 and also with the 5 terrestrial sites from Iberia included in the Kaufman et al. (2020) data set.
262 However, the patterns shown in the three data sets are very different from one another. Mauri
263 et al. (2015) suggest the early Holocene was colder than today, and although temperatures
264 similar to today were reached at 9 ka, most of the Holocene was characterised by cooler
265 summers. Kaufman et al. (2020), however, showed warmer than present conditions during the
266 early Holocene although they also show cooler conditions during the later Holocene. The
267 differences between the three data sets could reflect differences in the reconstruction methods,
268 or differences in the number of records used and in the geographic sampling. However, given
269 the fact that all three data sets show similar trends in winter temperature, the lack of coherency
270 between the data sets for MTWA points to there not being a strong, regionally coherent signal
271 of summer temperature changes during the Holocene. The differences between the three data
272 sets probably reflect differences in the number of records used, but the lack of coherency points
273 to there not being a strong, regionally coherent signal of summer temperature changes during
274 the Holocene. Tarroso et al. (2016) also showed no significant changes in MTWA after ca 9 ka
275 (SI Fig. S8 Fig. 7).

276 The chironomid record from Laguna de la Roya covers the late glacial and terminates at 10.5
277 ka (Muñoz Sobrino et al., 2013). The reconstructed July temperature during the early Holocene
278 is ca 12~13 °C, which is considerably cooler than today at this site. However, the authors
279 caution that these samples have poor analogues and the record should be interpreted with
280 caution. Chironomid-based reconstructions of July temperature at Basa de la Mora (Tarrats et
281 al., 2018), a high elevation site in the Pyrenees, indicate temperatures within $\pm 0.5^\circ \text{C}$ of the
282 modern during the early to mid-Holocene (10~6 ka), similar to our regional composite
283 reconstructions. However, they show persistently conditions cooler than present by ca 1.5 °C
284 between 4.5 and 2 ka, not seen in our reconstructions. Furthermore, direct comparison of our
285 reconstructions of MTWA at Basa de la Mora (SI Fig. S11 S9) to the chironomid-based
286 reconstructions highlights that the two records show very different trajectories, since the

287 pollen-based reconstruction of this site shows a consistent warming trend throughout the
288 Holocene. Although Tarrats et al. (2018) argue that discrepancies between their temperature
289 reconstructions and pollen-based reconstructions reflects the fact that the vegetation of Iberia,
290 including the mountain areas, is largely driven by moisture changes and perhaps is not a good
291 indicator of temperature, we have shown that there is sufficient information in the pollen
292 records to reconstruct temperature and moisture independently ([Table 2](#)[Table 3](#), [Table S](#)[Table](#)
293 [S22](#)). Thus, the cause of the differences between the pollen-based and chironomid-based
294 reconstructions at Basa de la Mora is presumably related to methodology. In particular, the
295 chironomid reconstructions use a training data set that does not include samples from the
296 Pyrenees, or indeed the Mediterranean more generally, and may therefore not provide good
297 analogues for Holocene changes at this site.

298 The lack of a clear trend in MTWA in our reconstructions is not consistent with insolation
299 forcing, which shows a declining trend during the Holocene nor is it consistent with simulated
300 changes in MTWA in transient climate model simulations (~~see supplementary materials for~~
301 ~~detailed description~~) of the summer temperature response to changing insolation forcing over
302 the Holocene in this region ([SI Fig. S9](#)[Fig. 8](#)). The change in moisture gradient during the mid-
303 Holocene, however, suggests an alternative explanation whereby changes in summer
304 temperature are a response to land-surface feedbacks associated with changes in moisture.
305 Specifically, the observed increased advection of moisture into eastern Iberia would have
306 created wetter conditions there, which in turn would permit increased evapotranspiration,
307 implying less allocation of available net radiation to sensible heating, and resulting in cooler
308 air temperatures. Our reconstructions show that the west-east moisture gradient in mid-
309 Holocene was significantly flatter than the steep moisture gradient today, implying a significant
310 increase in moisture advection into the continental interior during this period. Mauri et al.
311 (2015) also showed that summers were generally wetter than present in the east but drier than
312 present in the west at early to mid-Holocene, supporting the idea of a flatter west-east gradient.

313 We have shown that stronger moisture advection is not a feature of transient climate model
314 simulations of the Holocene, which may explain why these simulations do not show a strong
315 modification of the insolation-driven changes in summer temperature (Fig. [S98](#)). Although the
316 amplitude differs, all of the models show a general decline in summer temperature. The failure
317 of the current generation of climate models to simulate the observed strengthening of moisture
318 transport into Europe and Eurasia during the mid-Holocene has been noted for previous

319 versions of these models (e.g. Bartlein et al., 2017; Mauri et al., 2014) and also shown in Fig.
320 [S10S8](#). Mauri et al. (2014), for example, showed that climate models participating in the last
321 phase of the Coupled Model Intercomparison Project (CMIP5/PMIP3) were unable to
322 reproduce reconstructed climate patterns over Europe at 6000 yr B.P. and indicated that this
323 resulted from over-sensitivity to changes in insolation forcing and the failure to simulate
324 increased moisture transport into the continent. Bartlein et al. (2017) showed that the
325 CMIP5/PMIP3 models simulated warmer and drier conditions in mid-continental Eurasia at
326 6000 yr B.P., inconsistent with palaeo-environmental reconstructions from the region, as a
327 result of the simulated reduction in the zonal temperature gradient which resulted in weaker
328 westerly flow and reduced moisture fluxes into the mid-continent. They also pointed out the
329 strong feedback between drier conditions and summer temperatures. The drying of the mid-
330 continent is also a strong feature of the mid-Holocene simulations made with the current
331 generation of CMIP6/PMIP4 models (Brierley et al., 2020). The persistence of these data-
332 model mismatches highlights the need for better modelling of land-surface feedbacks on
333 atmospheric circulation and moisture.

334 There are comparatively few pollen-based reconstructions of moisture changes during the
335 Holocene from Iberia. Records from Padul show increased mean annual and winter
336 precipitation during the early and mid-Holocene (Camuera et al., 2022; García-Alix et al.,
337 2021). Reconstructions of mean annual and winter precipitation (Camuera et al., 2022) and the
338 ratio of annual precipitation to annual potential evapotranspiration (Wei et al., 2021) also show
339 wetter conditions at this time at El Cañizar de Villarquemado. Both of these sites lie in the
340 eastern part of the Iberian Peninsula, so these reconstructions are consistent with our
341 interpretation of wetter conditions in this region during the interval between 9.5 and 3.5 ka.
342 (Ilvonen et al., (2022) provide pollen-based reconstructions of mean annual, summer and
343 winter precipitation from 8 sites in Iberia, using WAPLS and a Bayesian modelling approach.
344 Although they focus on the contrasting pattern of hydroclimate evolution between northern and
345 southern Iberia, the three easternmost sites (San Rafael, Navarres, and Qintanar de la Sierra)
346 show much wetter conditions during the early to mid-Holocene. With the exception of the
347 record from Monte Areo, the records from further west are relatively complacent and indeed
348 two sites (Zalamar, El Maillo) show decreased precipitation between 8 and 4 ka. Thus, these
349 records are consistent with our interpretation that the west-east gradient of moisture was
350 reduced between 9.5 and 4.5 ka.

351 Speleothem oxygen-isotope data from the Iberian Peninsula provide support for our pollen-
352 based reconstructions of changes in the west-east gradient of moisture through the Holocene.
353 The speleothem records show a progressive increase in temperature from the Younger Dryas
354 onwards, although the trend is less marked in the west than the east (Baldini et al., 2019). This
355 warming trend is consistent with our reconstructions of changes in MTCO through the
356 Holocene. Speleothem records also show distinctly different patterns in moisture availability,
357 with sites in western Iberia indicating wetter environments during early Holocene and a
358 transition to drier conditions from ca 7.5 cal ka BP to the present (Stoll et al., 2013; Thatcher
359 et al., 2020) while eastern sites record wetter conditions persisting from 9 to 4 cal ka (Walczak
360 et al., 2015). This finding would support the weaker west to east moisture gradient shown by
361 our results.

362 Pollen data are widely used for the quantitative reconstruction of past climates (see discussion
363 in Bartlein et al., 2011), ~~but reconstructions of moisture indices are also affected by changes~~
364 ~~in water-use efficiency caused by the impact of changing atmospheric CO₂ levels on plant~~
365 ~~physiology (Farquhar, 1997; Gerhart and Ward, 2010; Prentice et al., 2017; Prentice and~~
366 ~~Harrison, 2009). This has been shown to be important on glacial-interglacial timescales, when~~
367 ~~intervals of lower-than-present CO₂ result in vegetation appearing to reflect drier conditions~~
368 ~~than were experienced in reality (Prentice et al., 2011, 2017; Wei et al., 2021). We do not~~
369 ~~account for this CO₂ effect in our reconstructions of α because the change in CO₂ over the~~
370 ~~Holocene was only 40 ppm. This change relative to modern levels has only a small impact on~~
371 ~~the reconstructions (Prentice et al., 2022) and is sufficiently small to be within the~~
372 ~~reconstruction uncertainties. Furthermore, accounting for changes in CO₂ would not affect the~~
373 ~~reconstructed west-east gradient through time.~~

374 ~~Nevertheless, climate is not the only driver of vegetation changes. On glacial-interglacial~~
375 ~~timescales, changes in CO₂ have a direct impact on plant physiological processes and~~
376 ~~reductions in plant water use efficiency at low CO₂ result in vegetation appearing to reflect~~
377 ~~drier conditions than were experienced in reality (Farquhar, 1997; Gerhart and Ward, 2010;~~
378 ~~Prentice et al., 2017; Prentice and Harrison, 2009). The difference between post and pre-~~
379 ~~industrial CO₂ levels could also influence the reliability of moisture reconstructions based on~~
380 ~~modern training data sets. However, the change in CO₂ over the Holocene was only 40 ppm.~~
381 ~~Prentice et al. (2022) shows that this change relative to modern levels has only a small impact~~
382 ~~on pollen-based reconstructed moisture indices. The magnitude of this impact is within the~~

383 ~~uncertainties on our reconstructions. Furthermore, accounting for the effect of this change in~~
384 ~~CO₂ or not won't affect the reconstructed west-east gradient through time. Therefore, we have~~
385 ~~not accounted for the impact of changing CO₂ in our reconstructions of α , although there are~~
386 ~~techniques to do this (Prentice et al., 2011, 2017; Wei et al., 2021). A more serious issue for~~
387 ~~our reconstructions may be the extent to which the vegetation cover of Iberia was substantially~~
388 ~~modified by human activities during the Holocene. While there is no doubt that anthropogenic~~
389 ~~activities were important at the local scale and particularly in the later Holocene (e.g. Abel-~~
390 ~~Schaad and López Sáez, 2013; Connor et al., 2019; Fyfe et al., 2019; Mighall et al., 2006;~~
391 ~~Revelles et al., 2015), most of the sites used for our reconstructions are not associated with~~
392 ~~archaeological evidence of agriculture or substantial landscape modification. Furthermore, the~~
393 ~~consistency of the reconstructed changes in climate across sites provides support for these~~
394 ~~being largely a reflection of regional climate changes. A more serious issue for our~~
395 ~~reconstructions may be the extent to which the vegetation cover of Iberia was substantially~~
396 ~~modified by human activities during the Holocene. Archaeological evidence shows that the~~
397 ~~introduction of agriculture during the Neolithic transition occurred ca 7.6 ka in some southern~~
398 ~~and eastern areas of the Iberian Peninsula but spread slowly and farming first occurred only~~
399 ~~around 6 ka in the northwest (Drake et al., 2017; Fyfe et al., 2019; Zapata et al., 2004).~~
400 ~~Anthropogenic changes in land use have been detected at a number of sites, based on pollen~~
401 ~~evidence of increases in weeds or the presence of cereals (e.g. Abel-Schaad and López-Sáez,~~
402 ~~2013; Cortés Sánchez et al., 2012; López-Merino et al., 2010; Mighall et al., 2006; Peña-~~
403 ~~Chocarro et al., 2005) or the presence of fungal spores associated with animal faeces which has~~
404 ~~been used to identify the presence of domesticated animals (e.g. López-Sáez and López-~~
405 ~~Merino, 2007; Revelles et al., 2018). The presence of cereals is the most reliable source of data~~
406 ~~on human activities, but most cereals only release pollen during threshing and thus are not~~
407 ~~found in abundance in pollen diagrams from natural (as opposed to archaeological) sites~~
408 ~~(Trondman et al., 2015). Indeed, it is only after ca 1 ka that the number of sites which record~~
409 ~~cereal pollen exceeds the number of sites at which cereals are not represented (Githumbi et al.,~~
410 ~~2022). Thus, while anthropogenic activities may have been important at the local scale and~~
411 ~~particularly in the later Holocene (e.g. Connor et al., 2019; Fyfe et al., 2019; Githumbi et al.,~~
412 ~~2022), most of the sites used for our reconstructions are not associated with archaeological~~
413 ~~evidence of agriculture or substantial landscape modification. Furthermore, the consistency of~~
414 ~~the reconstructed changes in climate across sites provides support for these being largely a~~
415 ~~reflection of regional climate changes rather than human activities.~~

416

417 We have used a modified version of fxTWA-PLS to reconstruct Holocene climates of the
418 Iberian Peninsula because this modification reduced the compression bias in MTCO and
419 MTWA, and specifically reduces the maximum bias in MTCO, MTWA and α . Although this
420 modified approach produces better overall reconstructions (Appendix A), its use does not
421 change the reconstructed trends in these variables through time (SI Fig. [S12S10](#)). Thus, the
422 finding that winter temperatures are a direct reflection of insolation forcing whereas summer
423 temperatures are influenced by land-surface feedbacks and changes in atmospheric circulation
424 is robust ~~to the~~ to the version of fxTWA-PLS used ~~method used~~. However, while we use a much
425 larger data set than previous reconstructions, the distribution of pollen sites is uneven and the
426 northern part of the Peninsula is better sampled than the southwest, which could lead to some
427 uncertainties in the interpretation of changes in the west-east gradient of moisture. It would,
428 therefore, be useful to specifically target the southwestern part of the Iberian Peninsula for new
429 data collection. Alternatively, it would be useful to apply the approach used here to the whole
430 of Eurasia, given that the failure of state-of-the-art climate models to advect moisture into the
431 continental interior appears to be a feature of the whole region (Bartlein et al., 2017) and not
432 the Peninsula alone.

433 5. Conclusion

434 We have developed an improved version of fxWA-PLS which further reduces compression
435 bias and provides robust climate reconstructions. We have used this technique with a large
436 pollen data set representing 117 sites across the Iberian Peninsula to make quantitative
437 reconstructions of summer and winter temperature and an index of plant-available moisture
438 through the Holocene. We show that there was a gradual increase in winter temperature through
439 the Holocene and that this trend broadly follows the changes in orbital forcing. Summer
440 temperatures, however, do not follow the changes in orbital forcing but appear to be influenced
441 by land-surface feedbacks associated with changes in moisture. We show that the west-east
442 gradient in moisture was considerably less pronounced during the mid-Holocene (8~4 ka),
443 implying a significant increase in moisture advection into the continental interior resulting from
444 changes in circulation. Our reconstructions of temperature changes are broadly consistent with
445 previous reconstructions, but are more solidly based because of the increased site coverage.
446 Our reconstructions of changes in the west-east gradient of moisture during the early part of
447 the Holocene are also consistent with previous reconstructions, although this change is not

448 simulated by state-of-the-art climate models, implying that there are still issues to resolve the
449 associated land-surface feedbacks in these models. Our work provides an improved foundation
450 for documenting and understanding the Holocene palaeoclimates of Iberia.

451 ~~We have used a pollen data set representing 117 sites across the Iberian Peninsula to make~~
452 ~~quantitative reconstructions of summer and winter temperature and an index of annual moisture~~
453 ~~through the Holocene. We show that the trends in winter temperature broadly follow the~~
454 ~~changes orbital forcing. Summer temperatures, however, do not follow the changes in orbital~~
455 ~~forcing but appear to be influenced by land surface feedbacks associated with changes in~~
456 ~~moisture. The west-east gradient in moisture was considerably less pronounced during the mid-~~
457 ~~Holocene (8-4 ka).~~

458

459 **Data and Code Availability**

460 All the data used are public access and cited here. The code used to generate the climate
461 reconstructions is available at <https://github.com/ml4418/Iberia-paper.git>.

462 **Supplement.** The supplement related to this article is available online.

463 **Competing interests.** We declare that we have no conflict of interest.

464 **Author Contributions.** ML, ICP and SPH designed the study. ML, ICP and CJFtB designed
465 the modifications to fxTWA-PLS. PG-S and GG-R provided pollen data and insights into the
466 regional palaeoclimate histories. ML carried out the analyses. ML and SPH wrote the first
467 draft of the paper and all authors contributed to the final draft.

468 **Acknowledgements.** ML acknowledges support from Imperial College through the Lee
469 Family Scholarship. YS and SPH acknowledge support from the ERC-funded project GC 2.0
470 (Global Change 2.0: Unlocking the past for a clearer future; grant number 694481). ICP
471 acknowledges support from the ERC under the European Union Horizon 2020 research and
472 innovation programme (grant agreement no: 787203 REALM). This work is a contribution to
473 the project "Origen y Cuantificación de los Cambios Paleoambientales en el Pirineo:
474 Variabilidad climática e impacto humano" (PYCACHU: PID2019-106050RB-I00)" funded by
475 the Ministerio de Ciencia e Innovación.

476 **Financial support.** This research has been supported by Lee Family Scholarship fund, and
477 the European Research Council (grant no. GC2.0, 694481, and grant no. REALM, 787203).

478 **References**

- 479 ~~Abel-Schaad, D., López-Sáez, J.A.: Vegetation changes in relation to fire history and human~~
480 ~~activities at the Peña Negra mire (Bejar Range, Iberian Central Mountain System, Spain)~~
481 ~~during the past 4,000 years. Veg. Hist. Archaeobot. 22, 199–214.~~
482 ~~<https://doi.org/10.1007/s00334-012-0368-9>, 2013.~~
- 483 Abel-Schaad, D. and López-Sáez, J. A.: Vegetation changes in relation to fire history and
484 human activities at the Peña Negra mire (Bejar Range, Iberian Central Mountain System,
485 Spain) during the past 4,000 years, Veg. Hist. Archaeobot., 22, 199–214,
486 doi:10.1007/s00334-012-0368-9, 2013.
- 487 Allison, P. D.: Multiple Regression: A Primer, Pine Forge Press., 1994.
- 488 Andrade, C., Contente, J. and Santos, J. A.: Climate change projections of aridity conditions
489 in the Iberian Peninsula, Water, 13(15), doi:10.3390/w13152035, 2021a.
- 490 Andrade, C., Contente, J. and Santos, J. A.: Climate change projections of dry and wet events
491 in Iberia based on the WASP-Index, Climate, 9(6), doi:10.3390/cli9060094, 2021b.
- 492 Aranbarri, J., Gonzalez Samperiz, P., Valero-Garcés, B., Moreno, A., Gil-Romera, G.,
493 Sevilla-Callejo, M., Garcia-Prieto, E., Di Rita, F., Mata, M. del Pi., Morellón, M., Magri, D.,
494 Rodríguez-Lazaro, J. and Carrión, J.: Rapid climatic changes and resilient vegetation during
495 the Lateglacial and Holocene in a continental region of south-western Europe, Glob. Planet.
496 Change, 114, 50–65, doi:10.1016/j.gloplacha.2014.01.003, 2014.
- 497 Aranbarri, J., González-Sampériz, P., Iriarte, E., Moreno, A., Rojo-Guerra, M., Peña-
498 Chocarro, L., Valero-Garcés, B., Leunda, M., García-Prieto, E., Sevilla-Callejo, M., Gil-
499 Romera, G., Magri, D. and Rodríguez-Lázaro, J.: Human–landscape interactions in the
500 Conquezueta–Ambrona Valley (Soria, continental Iberia): From the early Neolithic land use
501 to the origin of the current oak woodland, Palaeogeogr. Palaeoclimatol. Palaeoecol., 436, 41–
502 57, doi:<https://doi.org/10.1016/j.palaeo.2015.06.030>, 2015.
- 503 Baldini, L. M., Baldini, J. U. L., McDermott, F., Arias, P., Cueto, M., Fairchild, I. J.,
504 Hoffmann, D. L., Mathey, D. P., Müller, W., Nita, D. C., Ontañón, R., García-Moncó, C. and
505 Richards, D. A.: North Iberian temperature and rainfall seasonality over the Younger Dryas
506 and Holocene, Quat. Sci. Rev., 226, 105998,
507 doi:<https://doi.org/10.1016/j.quascirev.2019.105998>, 2019.
- 508 Bartlein, P. J., Prentice, I. C. and Webb, T.: Climatic response surfaces from pollen data for
509 some Eastern North American taxa, J. Biogeogr., 13(1), 35, doi:10.2307/2844848, 1986.
- 510 Bartlein, P. J., Harrison, S. P., Brewer, S., Connor, S., Davis, B. A. S., Gajewski, K., Guiot,
511 J., Harrison-Prentice, T. I., Henderson, A., Peyron, O., Prentice, I. C., Scholze, M., Seppä, H.,
512 Shuman, B., Sugita, S., Thompson, R. S., Vial, A. E., Williams, J. and Wu, H.: Pollen-based
513 continental climate reconstructions at 6 and 21 ka: A global synthesis, Clim. Dyn., 37(3),
514 775–802, doi:10.1007/s00382-010-0904-1, 2011.

- 515 Bartlein, P. J., Harrison, S. P. and Izumi, K.: Underlying causes of Eurasian midcontinental
516 aridity in simulations of mid-Holocene climate, *Geophys. Res. Lett.*, 44(17), 9020–9028,
517 doi:10.1002/2017GL074476, 2017.
- 518 Blaauw, M. and Christeny, J. A.: Flexible paleoclimate age-depth models using an
519 autoregressive gamma process, *Bayesian Anal.*, 6(3), 457–474, doi:10.1214/11-BA618, 2011.
- 520 Blaauw, M., Christen, J. A., Lopez, M. A. A. V., V., J. E. O. M. G., Belding, T., Theiler, J.,
521 Gough, B. and Karney, C.: rbacon: Age-depth modelling using Bayesian statistics, [online]
522 Available from: <https://cran.r-project.org/package=rbacon>, 2021.
- 523 ter Braak, C. J. F. and Juggins, S.: Weighted averaging partial least squares regression (WA-
524 PLS): An improved method for reconstructing environmental variables from species
525 assemblages, *Hydrobiologia*, 269(1), 485–502, doi:10.1007/BF00028046, 1993.
- 526 Braconnot, P., Crétat, J., Marti, O., Balkanski, Y., Caubel, A., Cozic, A., Foujols, M.-A. and
527 Sanogo, S.: Impact of multiscale variability on last 6,000 years Indian and West African
528 monsoon rain, *Geophys. Res. Lett.*, 46(23), 14021–14029,
529 doi:<https://doi.org/10.1029/2019GL084797>, 2019.
- 530 Brierley, C. M., Zhao, A., Harrison, S. P., Braconnot, P., Williams, C. J. R., Thornalley, D. J.
531 R., Shi, X., Peterschmitt, J.-Y., Ohgaito, R., Kaufman, D. S., Kageyama, M., Hargreaves, J.
532 C., Erb, M. P., Emile-Geay, J., D’Agostino, R., Chandan, D., Carré, M., Bartlein, P., Zheng,
533 W., Zhang, Z., Zhang, Q., Yang, H., Volodin, E. M., Tomas, R. A., Routsou, C., Peltier, W.
534 R., Otto-Bliesner, B., Morozova, P. A., McKay, N. P., Lohmann, G., Legrande, A. N., Guo,
535 C., Cao, J., Brady, E., Annan, J. D. and Abe-Ouchi, A.: Large-scale features and evaluation
536 of the PMIP4-CMIP6 midHolocene simulations, *Clim. Past Discuss.*, 2020, 1–35,
537 doi:10.5194/cp-2019-168, 2020.
- 538 Camuera, J., Ramos-Román, M. J., Jiménez-Moreno, G., García-Alix, A., Ilvonen, L., Ruha,
539 L., Gil-Romera, G., González-Sampériz, P. and Seppä, H.: Past 200 kyr hydroclimate
540 variability in the western Mediterranean and its connection to the African Humid Periods,
541 *Sci. Rep.*, 12(1), 9050, doi:10.1038/s41598-022-12047-1, 2022.
- 542 Carré, M., Braconnot, P., Elliot, M., d’Agostino, R., Schurer, A., Shi, X., Marti, O.,
543 Lohmann, G., Jungclaus, J., Cheddadi, R., Abdelkader di Carlo, I., Cardich, J., Ochoa, D.,
544 Salas Gismondi, R., Pérez, A., Romero, P. E., Turcq, B., Corrège, T. and Harrison, S. P.:
545 High-resolution marine data and transient simulations support orbital forcing of ENSO
546 amplitude since the mid-Holocene, *Quat. Sci. Rev.*, 268, 107125,
547 doi:<https://doi.org/10.1016/j.quascirev.2021.107125>, 2021.
- 548 Carrión, J. S., Fernández, S., González-Sampériz, P., Gil-Romera, G., Badal, E., Carrión-
549 Marco, Y., López-Merino, L., López-Sáez, J. A., Fierro, E. and Burjachs, F.: Expected trends
550 and surprises in the Lateglacial and Holocene vegetation history of the Iberian Peninsula and
551 Balearic Islands, *Rev. Palaeobot. Palynol.*, 162(3), 458–475,
552 doi:<https://doi.org/10.1016/j.revpalbo.2009.12.007>, 2010.

- 553 Carrión, Y., Kaal, J., López-Sáez, J. A., López-Merino, L. and Martínez Cortizas, A.:
 554 Holocene vegetation changes in NW Iberia revealed by anthracological and palynological
 555 records from a colluvial soil, *The Holocene*, 20(1), 53–66, doi:10.1177/0959683609348849,
 556 2009.
- 557 Carvalho, D., Pereira, S. and Rocha, A.: Future surface temperature changes for the Iberian
 558 Peninsula according to EURO-CORDEX climate projections, *Clim. Dyn.*, 56, 1–16,
 559 doi:10.1007/s00382-020-05472-3, 2021.
- 560 Cheddadi, R., Yu, G., Joel, G., Harrison, S., Prentice, I. and Colin, I.: The climate of Europe
 561 6000 years ago, *cd*, 13, 1, doi:10.1007/s003820050148, 1997.
- 562 Chevalier, M., Davis, B. A. S., Heiri, O., Seppä, H., Chase, B. M., Gajewski, K., Lacourse,
 563 T., Telford, R. J., Finsinger, W., Guiot, J., Köhl, N., Maezumi, S. Y., Tipton, J. R., Carter, V.
 564 A., Brussel, T., Phelps, L. N., Dawson, A., Zanon, M., Vallé, F., Nolan, C., Mauri, A., de
 565 Vernal, A., Izumi, K., Holmström, L., Marsicek, J., Goring, S., Sommer, P. S., Chaput, M.
 566 and Kupriyanov, D.: Pollen-based climate reconstruction techniques for late Quaternary
 567 studies, *Earth-Science Rev.*, 210, 103384,
 568 doi:https://doi.org/10.1016/j.earscirev.2020.103384, 2020.
- 569 Connor, S., Vannièrè, B., Colombaroli, D., Anderson, R., Carrión, J., Ejarque, A., Gil-
 570 Romera, G., Gonzalez Samperiz, P., Höfer, D., Morales-Molino, C., Revelles, J., Schneider,
 571 H., Knaap, W., Leeuwen, J. and Woodbridge, J.: Humans take control of fire-driven diversity
 572 changes in Mediterranean Iberia's vegetation during the mid-late Holocene, *The Holocene*,
 573 29, 095968361982665, doi:10.1177/0959683619826652, 2019.
- 574 Cortés Sánchez, M., Jiménez Espejo, F. J., Simón Vallejo, M. D., Gibaja Bao, J. F., Carvalho,
 575 A. F., Martínez-Ruiz, F., Gamiz, M. R., Flores, J.-A., Paytan, A., López Sáez, J. A., Peña-
 576 Chocarro, L., Carrión, J. S., Morales Muñiz, A., Roselló Izquierdo, E., Riquelme Cantal, J.
 577 A., Dean, R. M., Salgueiro, E., Martínez Sánchez, R. M., De la Rubia de Gracia, J. J., Lozano
 578 Francisco, M. C., Vera Peláez, J. L., Rodríguez, L. L. and Bicho, N. F.: The Mesolithic–
 579 Neolithic transition in southern Iberia, *Quat. Res.*, 77(2), 221–234,
 580 doi:https://doi.org/10.1016/j.yqres.2011.12.003, 2012.
- 581 Dallmeyer, A., Claussen, M., Lorenz, S. J. and Shanahan, T.: The end of the African humid
 582 period as seen by a transient comprehensive Earth system model simulation of the last 8000
 583 years, , doi:10.5194/cp-2019-86, 2020.
- 584 Davis, B. A. S., Brewer, S., Stevenson, A. C. and Guiot, J.: The temperature of Europe during
 585 the Holocene reconstructed from pollen data, *Quat. Sci. Rev.*, 22(15), 1701–1716,
 586 doi:https://doi.org/10.1016/S0277-3791(03)00173-2, 2003.
- 587 Davis, T. W., Prentice, I. C., Stocker, B. D., Thomas, R. T., Whitley, R. J., Wang, H., Evans,
 588 B. J., Gallego-Sala, A. V., Sykes, M. T. and Cramer, W.: Simple process-led algorithms for
 589 simulating habitats (SPLASH v.1.0): Robust indices of radiation, evapotranspiration and
 590 plant-available moisture, *Geosci. Model Dev.*, 10(2), 689–708, doi:10.5194/gmd-10-689-
 591 2017, 2017.

- 592 Drake, B. L., Blanco-González, A. and Lillios, K. T.: Regional Demographic Dynamics in
 593 the Neolithic Transition in Iberia: Results from Summed Calibrated Date Analysis, *J.*
 594 *Archaeol. Method Theory*, 24(3), 796–812, doi:10.1007/s10816-016-9286-y, 2017.
- 595 Eilers, P. H. and Marx, B. D.: *Practical smoothing: The Joys of P-splines*, edited by P. H.
 596 Eilers and B. D. Marx, Cambridge University Press., 2021.
- 597 Farquhar, G. D.: Carbon dioxide and vegetation, *Science* (80-), 278(5342), 1411,
 598 doi:10.1126/science.278.5342.1411, 1997.
- 599 Fyfe, R. M., Woodbridge, J., Palmisano, A., Bevan, A., Shennan, S., Burjachs, F., Legarra
 600 Herrero, B., García Puchol, O., Carrión, J. S., Revelles, J. and Roberts, C. N.: Prehistoric
 601 palaeodemographics and regional land cover change in eastern Iberia, *Holocene*, 29(5), 799–
 602 815, doi:10.1177/0959683619826643, 2019.
- 603 García-Alix, A., Camuera, J., Ramos-Román, M. J., Toney, J. L., Sachse, D., Schefuß, E.,
 604 Jiménez-Moreno, G., Jiménez-Espejo, F. J., López-Avilés, A., Anderson, R. S. and Yanes,
 605 Y.: Paleohydrological dynamics in the Western Mediterranean during the last glacial cycle,
 606 *Glob. Planet. Change*, 202, 103527, doi:https://doi.org/10.1016/j.gloplacha.2021.103527,
 607 2021.
- 608 Gerhart, L. M. and Ward, J. K.: Plant responses to low [CO₂] of the past, *New Phytol.*,
 609 188(3), 674–695, doi:https://doi.org/10.1111/j.1469-8137.2010.03441.x, 2010.
- 610 Githumbi, E., Fyfe, R., Gaillard, M.-J., Trondman, A.-K., Mazier, F., Nielsen, A.-B., Poska,
 611 A., Sugita, S., Woodbridge, J., Azuara, J., Feurdean, A., Grindean, R., Lebreton, V.,
 612 Marquer, L., Nebout-Combourieu, N., Stančikaitė, M., Tanțuau, I., Tonkov, S.,
 613 Shumilovskikh, L. and data contributors, L.: European pollen-based REVEALS land-cover
 614 reconstructions for the Holocene: methodology, mapping and potentials, *Earth Syst. Sci.*
 615 *Data*, 14(4), 1581–1619, doi:10.5194/essd-14-1581-2022, 2022.
- 616 González-Sampériz, P., Aranbarri, J., Pérez-Sanz, A., Gil-Romera, G., Moreno, A., Leunda,
 617 M., Sevilla-Callejo, M., Corella, J. P., Morellón, M., Oliva, B. and Valero-Garcés, B.:
 618 Environmental and climate change in the southern Central Pyrenees since the Last Glacial
 619 Maximum: A view from the lake records, *Catena*, 149, 668–688,
 620 doi:https://doi.org/10.1016/j.catena.2016.07.041, 2017.
- 621 Granados, I. and Toro, M.: Recent warming in a high mountain lake (Laguna Cimera, Central
 622 Spain) inferred by means of fossil chironomids, *J. Limnol.*, 59 (suppl.), 109–119,
 623 doi:10.4081/jlimnol.2000.s1.109, 2000.
- 624 Hammer, O., Harper, D. and Ryan, P.: PAST: Paleontological statistics software package for
 625 education and data analysis, *Palaeontol. Electron.*, 4, 1–9, 2001.
- 626 Harrison, S., Shen, Y. and Sweeney, L.: Pollen data and charcoal data of the Iberian
 627 Peninsula (version 3), [online] Available from: https://doi.org/10.17864/1947.000369, 2022.

- 628 Harrison, S. P.: Modern pollen data for climate reconstructions, version 1 (SMPDS), ,
629 doi:<http://dx.doi.org/10.17864/1947.194>, 2019.
- 630 Holden, P. B., Birks, H. J. B., Brooks, S. J., Bush, M. B., Hwang, G. M., Matthews-Bird, F.,
631 Valencia, B. G. and van Woesik, R.: BUMPER v1.0: a Bayesian user-friendly model for
632 palaeo-environmental reconstruction, *Geosci. Model Dev.*, 10(1), 483–498,
633 doi:[10.5194/gmd-10-483-2017](https://doi.org/10.5194/gmd-10-483-2017), 2017.
- 634 Ilvonen, L., López-Sáez, J. A., Holmström, L., Alba-Sánchez, F., Pérez-Díaz, S., Carrión, J.
635 S., Ramos-Román, M. J., Camuera, J., Jiménez-Moreno, G., Ruha, L. and Seppä, H.: Spatial
636 and temporal patterns of Holocene precipitation change in the Iberian Peninsula, *Boreas*,
637 doi:<https://doi.org/10.1111/bor.12586>, 2022.
- 638 Kaufman, D., McKay, N., Routson, C., Erb, M., Davis, B., Heiri, O., Jaccard, S., Tierney, J.,
639 Dätwyler, C., Axford, Y., Brussel, T., Cartapanis, O., Chase, B., Dawson, A., de Vernal, A.,
640 Engels, S., Jonkers, L., Marsicek, J., Moffa-Sánchez, P., Morrill, C., Orsi, A., Rehfeld, K.,
641 Saunders, K., Sommer, P. S., Thomas, E., Tonello, M., Tóth, M., Vachula, R., Andreev, A.,
642 Bertrand, S., Biskaborn, B., Bringué, M., Brooks, S., Caniupán, M., Chevalier, M., Cwynar,
643 L., Emile-Geay, J., Fegyveresi, J., Feurdean, A., Finsinger, W., Fortin, M.-C., Foster, L., Fox,
644 M., Gajewski, K., Grosjean, M., Hausmann, S., Heinrichs, M., Holmes, N., Ilyashuk, B.,
645 Ilyashuk, E., Juggins, S., Khider, D., Koinig, K., Langdon, P., Larocque-Tobler, I., Li, J.,
646 Lotter, A., Luoto, T., Mackay, A., Magyari, E., Malevich, S., Mark, B., Massaferrro, J.,
647 Montade, V., Nazarova, L., Novenko, E., Pařil, P., Pearson, E., Peros, M., Pienitz, R.,
648 Płóciennik, M., Porinchu, D., Potito, A., Rees, A., Reinemann, S., Roberts, S., Rolland, N.,
649 Salonen, S., Self, A., Seppä, H., Shala, S., St-Jacques, J.-M., Stenni, B., Strykh, L., Tarrats,
650 P., Taylor, K., van den Bos, V., Velle, G., Wahl, E., Walker, I., Wilmshurst, J., Zhang, E. and
651 Zhilich, S.: A global database of Holocene paleotemperature records, *Sci. Data*, 7(1), 115,
652 doi:[10.1038/s41597-020-0445-3](https://doi.org/10.1038/s41597-020-0445-3), 2020.
- 653 Liu, M., Prentice, I. C., ter Braak, C. J. F. and Harrison, S. P.: An improved statistical
654 approach for reconstructing past climates from biotic assemblages, *Proc. R. Soc. A Math.*,
655 476(2243), doi:<https://doi.org/10.1098/rspa.2020.0346>, 2020.
- 656 López-Merino, L., Cortizas, A. M. and López-Sáez, J. A.: Early agriculture and
657 palaeoenvironmental history in the North of the Iberian Peninsula: a multi-proxy analysis of
658 the Monte Areo mire (Asturias, Spain), *J. Archaeol. Sci.*, 37(8), 1978–1988,
659 doi:<https://doi.org/10.1016/j.jas.2010.03.003>, 2010.
- 660 López-Sáez, J. A. and López-Merino, L.: Coprophilous fungi as a source of information of
661 anthropic activities during the Prehistory in the Amblés Valley (Ávila, Spain): The
662 archaeopalynological record, *Rev. Española Micropaleontol.*, 38, 49–75, 2007.
- 663 Martínez-Cortizas, A., Costa-Casais, M. and López-Sáez, J. A.: Environmental change in
664 NW Iberia between 7000 and 500cal BC, *Quat. Int.*, 200(1), 77–89,
665 doi:<https://doi.org/10.1016/j.quaint.2008.07.012>, 2009.
- 666 Mauri, A., Davis, B. A. S., Collins, P. M. and Kaplan, J. O.: The influence of atmospheric
667 circulation on the mid-Holocene climate of Europe: a data–model comparison, *Clim. Past*,

- 668 10(5), 1925–1938, doi:10.5194/cp-10-1925-2014, 2014.
- 669 Mauri, A., Davis, B. A. S., Collins, P. M. and Kaplan, J. O.: The climate of Europe during the
670 Holocene: A gridded pollen-based reconstruction and its multi-proxy evaluation, *Quat. Sci.*
671 *Rev.*, 112, 109–127, doi:10.1016/j.quascirev.2015.01.013, 2015.
- 672 Mighall, T. M., Martínez Cortizas, A., Biester, H. and Turner, S. E.: Proxy climate and
673 vegetation changes during the last five millennia in NW Iberia: Pollen and non-pollen
674 palynomorph data from two ombrotrophic peat bogs in the North Western Iberian Peninsula,
675 *Rev. Palaeobot. Palynol.*, 141(1–2), 203–223, doi:10.1016/j.revpalbo.2006.03.013, 2006.
- 676 Millet, L., Rius, D., Galop, D., Heiri, O. and Brooks, S. J.: Chironomid-based reconstruction
677 of Lateglacial summer temperatures from the Ech palaeolake record (French western
678 Pyrenees), *Palaeogeogr. Palaeoclimatol. Palaeoecol.*, 315–316, 86–99,
679 doi:<https://doi.org/10.1016/j.palaeo.2011.11.014>, 2012.
- 680 Morellón, M., Aranbarri, J., Moreno, A., González-Sampériz, P. and Valero-Garcés, B. L.:
681 Early Holocene humidity patterns in the Iberian Peninsula reconstructed from lake, pollen
682 and speleothem records, *Quat. Sci. Rev.*, 181, 1–18,
683 doi:<https://doi.org/10.1016/j.quascirev.2017.11.016>, 2018.
- 684 Muñoz Sobrino, C., Heiri, O., Hazekamp, M., van der Velden, D., Kirilova, E. P., García-
685 Moreiras, I. and Lotter, A. F.: New data on the Lateglacial period of SW Europe: a high
686 resolution multiproxy record from Laguna de la Roya (NW Iberia), *Quat. Sci. Rev.*, 80, 58–
687 77, doi:<https://doi.org/10.1016/j.quascirev.2013.08.016>, 2013.
- 688 New, M., Lister, D. and Hulme, M.: A high-resolution data set of surface climate over global
689 land areas, *Clim. Res.*, 21(1), 1–25 [online] Available from: [http://www.int-](http://www.int-res.com/abstracts/cr/v21/n1/p1-25/)
690 [res.com/abstracts/cr/v21/n1/p1-25/](http://www.int-res.com/abstracts/cr/v21/n1/p1-25/), 2002.
- 691 Overpeck, J. T., Webb, T. and Prentice, I. C.: Quantitative interpretation of fossil pollen
692 spectra: Dissimilarity coefficients and the method of modern analogs, *Quat. Res.*, 23(1), 87–
693 108, doi:10.1016/0033-5894(85)90074-2, 1985.
- 694 Parker, S. E., Harrison, S. P. and Braconnot, P.: Speleothem records of monsoon interannual-
695 interdecadal variability through the Holocene, *Environ. Res. Commun.*, 3(12), 121002,
696 doi:10.1088/2515-7620/ac3eaa, 2021.
- 697 Peña-Chocarro, L., Peña, L. Z., Gazólaz, J. G., Morales, M. G., Sesma, J. S. and Straus, L.
698 G.: The spread of agriculture in northern Iberia: new archaeobotanical data from El Mirón
699 cave (Cantabria) and the open-air site of Los Cascajos (Navarra), *Veg. Hist. Archaeobot.*,
700 14(4), 268–278, doi:10.1007/s00334-005-0078-7, 2005.
- 701 Peyron, O., Guiot, J., Cheddadi, R., Tarasov, P., Reille, M., de Beaulieu, J.-L., Bottema, S.
702 and Andrieu, V.: Climatic reconstruction in Europe for 18,000 yr B.P. from pollen data, *Quat.*
703 *Res.*, 49(2), 183–196, doi:<https://doi.org/10.1006/qres.1997.1961>, 1998.

- 704 Prentice, I. C. and Harrison, S. P.: Ecosystem effects of CO₂ concentration: evidence from
705 past climates, *Clim. Past*, 5(3), 297–307, doi:10.5194/cp-5-297-2009, 2009.
- 706 Prentice, I. C., Meng, T., Wang, H., Harrison, S. P., Ni, J. and Wang, G.: Evidence of a
707 universal scaling relationship for leaf CO₂ drawdown along an aridity gradient, *New Phytol.*,
708 190(1), 169–180, doi:https://doi.org/10.1111/j.1469-8137.2010.03579.x, 2011.
- 709 Prentice, I. C., Cleator, S. F., Huang, Y. H., Harrison, S. P. and Roulstone, I.: Reconstructing
710 ice-age palaeoclimates: Quantifying low-CO₂ effects on plants, *Glob. Planet. Change*, 149,
711 166–176, doi:https://doi.org/10.1016/j.gloplacha.2016.12.012, 2017.
- 712 Prentice, I. C., Villegas-Diaz, R. and Harrison, S. P.: Accounting for atmospheric carbon
713 dioxide variations in pollen-based reconstruction of past hydroclimates, *Glob. Planet.*
714 *Change*, 2022.
- 715 Ramos-Román, M. J., Jiménez-Moreno, G., Camuera, J., García-Alix, A., Anderson, R.,
716 Jiménez-Espejo, F., Sachse, D., Jaime, T., Carrión, J., Webster, C. and Yanes, Y.: Millennial-
717 scale cyclical environment and climate variability during the Holocene in the western
718 Mediterranean region deduced from a new multi-proxy analysis from the Padul record (Sierra
719 Nevada, Spain), *Glob. Planet. Change*, 168, doi:10.1016/j.gloplacha.2018.06.003, 2018.
- 720 Reimer, P. J., Austin, W. E. N., Bard, E., Bayliss, A., Blackwell, P. G., Bronk Ramsey, C.,
721 Butzin, M., Cheng, H., Edwards, R. L., Friedrich, M., Grootes, P. M., Guilderson, T. P.,
722 Hajdas, I., Heaton, T. J., Hogg, A. G., Hughen, K. A., Kromer, B., Manning, S. W.,
723 Muscheler, R., Palmer, J. G., Pearson, C., Van Der Plicht, J., Reimer, R. W., Richards, D. A.,
724 Scott, E. M., Southon, J. R., Turney, C. S. M., Wacker, L., Adolphi, F., Büntgen, U., Capano,
725 M., Fahrni, S. M., Fogtmann-Schulz, A., Friedrich, R., Köhler, P., Kudsk, S., Miyake, F.,
726 Olsen, J., Reinig, F., Sakamoto, M., Sookdeo, A. and Talamo, S.: The IntCal20 Northern
727 Hemisphere radiocarbon age calibration curve (0-55 cal kBP), *Radiocarbon*, 62(4), 725–757,
728 doi:10.1017/RDC.2020.41, 2020.
- 729 Revelles, J., Burjachs, F., Palomo, A., Piqué, R., Iriarte, E., Pérez-Obiol, R. and Terradas, X.:
730 Human-environment interaction during the Mesolithic- Neolithic transition in the NE Iberian
731 Peninsula. Vegetation history, climate change and human impact during the Early-Middle
732 Holocene in the Eastern Pre-Pyrenees, *Quat. Sci. Rev.*, 184, 183–200,
733 doi:https://doi.org/10.1016/j.quascirev.2017.08.025, 2018.
- 734 Salonen, J. S., Ilvonen, L., Seppä, H., Holmström, L., Telford, R. J., Gaidamavičius, A.,
735 Stančikaitė, M. and Subetto, D.: Comparing different calibration methods (WA/WA-PLS
736 regression and Bayesian modelling) and different-sized calibration sets in pollen-based
737 quantitative climate reconstruction, *The Holocene*, 22(4), 413–424,
738 doi:10.1177/0959683611425548, 2011.
- 739 Salonen, J. S., Korpela, M., Williams, J. W. and Luoto, M.: Machine-learning based
740 reconstructions of primary and secondary climate variables from North American and
741 European fossil pollen data, *Sci. Rep.*, 9(1), 15805, doi:10.1038/s41598-019-52293-4, 2019.

- 742 Schröder, T., López-Sáez, J. A., van't Hoff, J. and Reicherter, K.: Unravelling the Holocene
 743 environmental history of south-western Iberia through a palynological study of Lake Medina
 744 sediments, *The Holocene*, 30(1), 13–22, doi:10.1177/0959683619865590, 2019.
- 745 Shen, Y., Sweeney, L., Liu, M., Lopez Saez, J. A., Pérez-Díaz, S., Luelmo-Lautenschlaeger,
 746 R., Gil-Romera, G., Hoefler, D., Jiménez-Moreno, G., Schneider, H., Prentice, I. C. and
 747 Harrison, S. P.: Reconstructing burnt area during the Holocene: an Iberian case study, *Clim.*
 748 *Past*, 18, 1189–1201, doi:10.5194/cp-2021-36, 2022.
- 749 Stoll, H. M., Moreno, A., Mendez-Vicente, A., Gonzalez-Lemos, S., Jimenez-Sanchez, M.,
 750 Dominguez-Cuesta, M. J., Edwards, R. L., Cheng, H. and Wang, X.: Paleoclimate and
 751 growth rates of speleothems in the northwestern Iberian Peninsula over the last two glacial
 752 cycles, *Quat. Res.*, 80, 284–290, doi:10.1016/j.yqres.2013.05.002, 2013.
- 753 Tarrats, P., Heiri, O., Valero-Garcés, B., Cañedo-Argüelles, M., Prat, N., Rieradevall, M. and
 754 González-Sampériz, P.: Chironomid-inferred Holocene temperature reconstruction in Basa de
 755 la Mora Lake (Central Pyrenees), *The Holocene*, 28(11), 1685–1696,
 756 doi:10.1177/0959683618788662, 2018.
- 757 Tarroso, P., Carrión, J., Dorado-Valiño, M., Queiroz, P., Santos, L., Valdeolmillos-
 758 Rodríguez, A., Célio Alves, P., Brito, J. C. and Cheddadi, R.: Spatial climate dynamics in the
 759 Iberian Peninsula since 15 000 yr BP, *Clim. Past*, 12(5), 1137–1149, doi:10.5194/cp-12-
 760 1137-2016, 2016.
- 761 Thatcher, D. L., Wanamaker, A. D., Denniston, R. F., Asmerom, Y., Polyak, V. J., Fullick,
 762 D., Ummenhofer, C. C., Gillikin, D. P. and Haws, J. A.: Hydroclimate variability from
 763 western Iberia (Portugal) during the Holocene: Insights from a composite stalagmite isotope
 764 record, *The Holocene*, 30(7), 966–981, doi:https://doi.org/10.1177/0959683620908648,
 765 2020.
- 766 Trondman, A.-K., Gaillard, M.-J., Mazier, F., Sugita, S., Fyfe, R., Nielsen, A. B., Twiddle,
 767 C., Barratt, P., Birks, H. J. B., Bjune, A. E., Björkman, L., Broström, A., Caseldine, C.,
 768 David, R., Dodson, J., Dörfler, W., Fischer, E., van Geel, B., Giesecke, T., Hultberg, T.,
 769 Kalnina, L., Kangur, M., van der Knaap, P., Koff, T., Kuneš, P., Lagerås, P., Latałowa, M.,
 770 Lechterbeck, J., Leroyer, C., Leydet, M., Lindbladh, M., Marquer, L., Mitchell, F. J. G.,
 771 Odgaard, B. V., Peglar, S. M., Persson, T., Poska, A., Rösch, M., Seppä, H., Veski, S. and
 772 Wick, L.: Pollen-based quantitative reconstructions of Holocene regional vegetation cover
 773 (plant-functional types and land-cover types) in Europe suitable for climate modelling, *Glob.*
 774 *Chang. Biol.*, 21(2), 676–697, doi:https://doi.org/10.1111/gcb.12737, 2015.
- 775 Villegas-Diaz, Roberto; Cruz-Silva, Esmeralda; Harrison, S. P.: ageR: Supervised age
 776 models, , doi:10.5281/zenodo.4636715, 2021.
- 777 Walczak, I. W., Baldini, J. U. L., Baldini, L. M., McDermott, F., Marsden, S., Standish, C.
 778 D., Richards, D. A., Andreo, B. and Slater, J.: Reconstructing high-resolution climate using
 779 CT scanning of unsectioned stalagmites: A case study identifying the mid-Holocene onset of
 780 the Mediterranean climate in southern Iberia, *Quat. Sci. Rev.*, 127, 117–128,
 781 doi:https://doi.org/10.1016/j.quascirev.2015.06.013, 2015.

782 Wei, D., González-Sampériz, P., Gil-Romera, G., Harrison, S. P. and Prentice, I. C.: Seasonal
783 temperature and moisture changes in interior semi-arid Spain from the last interglacial to the
784 Late Holocene, *Quat. Res.*, 101, 143–155, doi:DOI: 10.1017/qua.2020.108, 2021.

785 Wu, H., Guiot, J., Brewer, S. and Guo, Z.: Climatic changes in Eurasia and Africa at the last
786 glacial maximum and mid-Holocene: reconstruction from pollen data using inverse
787 vegetation modelling, *Clim. Dyn.*, 29(2), 211–229, doi:10.1007/s00382-007-0231-3, 2007.

788 Zapata, L., Peña-Chocarro, L., Pérez-Jordá, G. and Stika, H.-P.: Early Neolithic Agriculture
789 in the Iberian Peninsula, *J. World Prehistory*, 18(4), 283–325 [online] Available from:
790 <http://www.jstor.org/stable/25801225>, 2004.

791

792 **Figure and Table Captions**

793 Figure 1. Climate space represented by mean temperature of the coldest month (MTCO),
 794 mean temperature of the warmest month (MTWA), and plant-available moisture as
 795 represented by α , an estimate of the ratio of actual evapotranspiration to equilibrium
 796 evapotranspiration. The grey points show climate values for a rectangular area (21° W ~ 150°
 797 E, 29° N ~ 82° N) enclosing the SMPDS data set, derived from the Climate Research Unit
 798 CRU CL 2.0 database (New et al., 2002). The black points show climate values of the
 799 SMPDS dataset. The red points show climate values of the Iberian Peninsula region in the
 800 SMPDS dataset.

801 Figure 2. Map showing the location of the 117 fossil sites in the Iberian Peninsula used for
 802 climate reconstructions. Sites lower than 1000 ~~m a.s.l. m above sea level~~ are shown as
 803 squares, sites higher than 1000 ~~m m a.s.l. above sea level~~ are shown as triangles. The base
 804 maps show modern (a) mean temperature of the coldest month (MTCO), (b) mean
 805 temperature of the warmest month (MTWA), and (c) plant-available moisture as represented
 806 by α , an estimate of the ratio of actual evapotranspiration to equilibrium evapotranspiration.

807 Figure 3. Reconstructed anomalies in climate at individual sites through time. The sites are
 808 grouped into high (>1000m) and low (<1000m) elevation sites and organised from west to east.
 809 Grey cells indicate periods or longitudes with no data. The individual plots show the anomalies
 810 in reconstructed (a,d) mean temperature of the coldest month (MTCO), (b,e) mean temperature
 811 of the warmest month (MTWA), and (c,f) plant-available moisture as represented by α , an
 812 estimate of the ratio of actual evapotranspiration to equilibrium evapotranspiration. The
 813 anomalies are expressed as deviations of the mean value in each bin (± 500 years) from the
 814 value at 0.5 ka at each site.

815 Figure 4. Reconstructed composite changes (anomalies to 0.5 ka) in (a) mean temperature of
 816 the coldest month (MTCO), (b) mean temperature of the warmest month (MTWA) and (c)
 817 plant-available moisture as represented by α , through the Holocene compared to changes in
 818 (d) winter and (e) summer insolation for the latitude of the Iberian Peninsula, using ± 500
 819 years as the bin. The black lines show mean values across sites, with vertical line segments
 820 showing the standard deviations of mean values using 1000 bootstrap cycles of site
 821 resampling.

822 Figure 5. Changes in the west-east gradient of plant-available moisture as represented by
 823 anomalies in α relative to 0.5 ka at individual sites through the Holocene. The red lines show
 824 the regression lines. The shades indicate the 95 % confidence intervals of the regression lines

825 Figure 6. The relationship between mean temperature of the warmest month (MTWA) and
 826 plant-available moisture as represented by α (a) in the modern climate data set, and (b) in the
 827 Holocene reconstructions.

828 Figure 7. Comparison between reconstructed composite changes in climate anomalies. The first
 829 column represents this paper, the second column represents Mauri et al. (2015), the third
 830 column represents Kaufman et al. (2020), the fourth column represents Tarroso et al. (2016).
 831 The composite curves from this paper and Kaufman et al. (2020) are calculated from individual
 832 reconstructions, using anomalies to 0.5 ka and a bin of ± 500 years (time slices are 0.5, 1.5, ...,
 833 11.5 ka). The composite curves from Mauri et al. (2015) are converted directly from the gridded
 834 time slices which are provided with anomalies to 0.1 ka and a bin of ± 500 years (time slices
 835 are 1, 2, ..., 12 ka). The composite curves from Tarroso et al. (2016) are also converted directly
 836 from the gridded time slices provided, with anomalies to 0.5 ka and a bin of ± 500 years (time
 837 slices are 3, 4, ..., 12 ka). Note that Tarroso et al. (2016) applied a smoothing to the data such
 838 that the plots in the paper do not show the excursion in MTWA at 8 ka. In all of the plots, the
 839 black lines show mean values across sites, with vertical line bars showing the standard
 840 deviation of mean values using 1000 bootstrap cycles of site/grid resampling.

841 Figure 8. Simulated mean values of mean temperature of the coldest month (MTCO), mean
 842 temperature of the warmest month (MTWA) and mean daily precipitation in Iberian Peninsula
 843 between 8 ka and 0 ka, smoothed using 100 year bins. Here BP means before 1950 AD. The
 844 black lines represent Max Planck Institute Earth System Model (MPI) simulations, the red lines
 845 represent Alfred Wagner Insitute Earth System Model (AWI) simulations, the blue lines
 846 represent Institut Pierre Simon Laplace Climate Model (IPSL-CM5) TR5AS simulations, the
 847 orange lines represent Institut Pierre Simon Laplace Climate Model (IPSL-CM6) TR6AV
 848 simulations. The four simulations were forced by evolving orbital parameters and greenhouse
 849 gas concentrations. The four models have different spatial resolution, with the finest resolution
 850 being $1.875^\circ \times 1.875^\circ$ (AWI, MPI) and the coarsest resolution being $1.875^\circ \times 3.75^\circ$ (IPSL-
 851 CM5, TR5AS).

852 Table 1. Details of the fossil pollen sites used. The fossil pollen data from the Iberian
 853 Peninsula were compiled by Shen et al. (2021) and obtained from
 854 <https://doi.org/10.17864/1947.000343>. The reference list of this table can be found in the
 855 supplementary.

856

857 ~~Table 1~~ Table 2. Leave-out cross-validation (with geographically and climatically close sites
 858 removed) fitness of the modified version of fxTWA-PLS, for mean temperature of the coldest
 859 month (MTCO), mean temperature of the warmest month (MTWA) and plant-available
 860 moisture (α), with p-spline smoothed fx estimation, using bins of 0.02, 0.02 and 0.002,

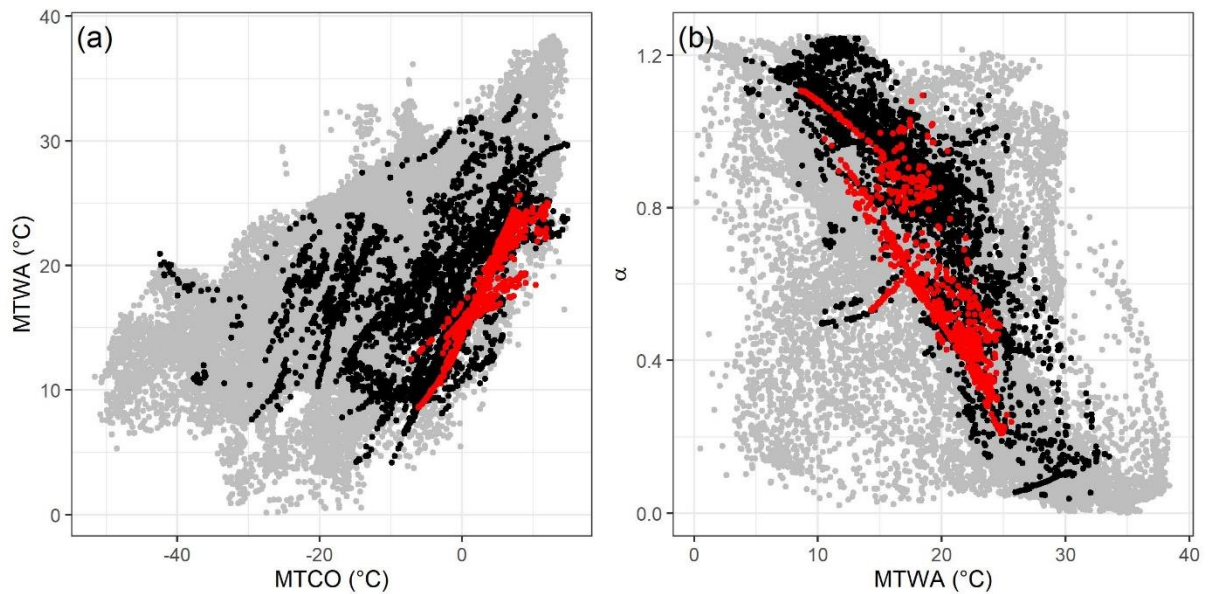
861 showing results for all the components. RMSEP is the root-mean-square error of prediction.
862 Δ RMSEP is the per cent change of RMSEP using the current number of components than
863 using one component less. p assesses whether using the current number of components is
864 significantly different from using one component less, which is used to choose the last
865 significant number of components (indicated in bold) to avoid over-fitting. The degree of
866 overall compression is assessed by linear regression of the cross-validated reconstructions
867 onto the climate variable, b_1 , $b_1.se$ are the slope and the standard error of the slope,
868 respectively. The closer the slope (b_1) is to 1, the less the overall compression is.

869 ~~Table 2~~Table 3. Canonical Correspondence Analysis (CCA) result of modern and fossil-
870 reconstructed MTCO, MTWA and α . The summary statistics for the ANOVA-like
871 permutation test (999 permutations) are also shown. VIF is the variance inflation factor, Df is
872 the number of degrees of freedom, χ^2 is the constrained eigenvalue (or the sum of constrained
873 eigenvalues for the whole model), F is significance, and Pr (>F) is the probability. The CCA
874 plots can be found in the Supplementary (Fig. S11).

875

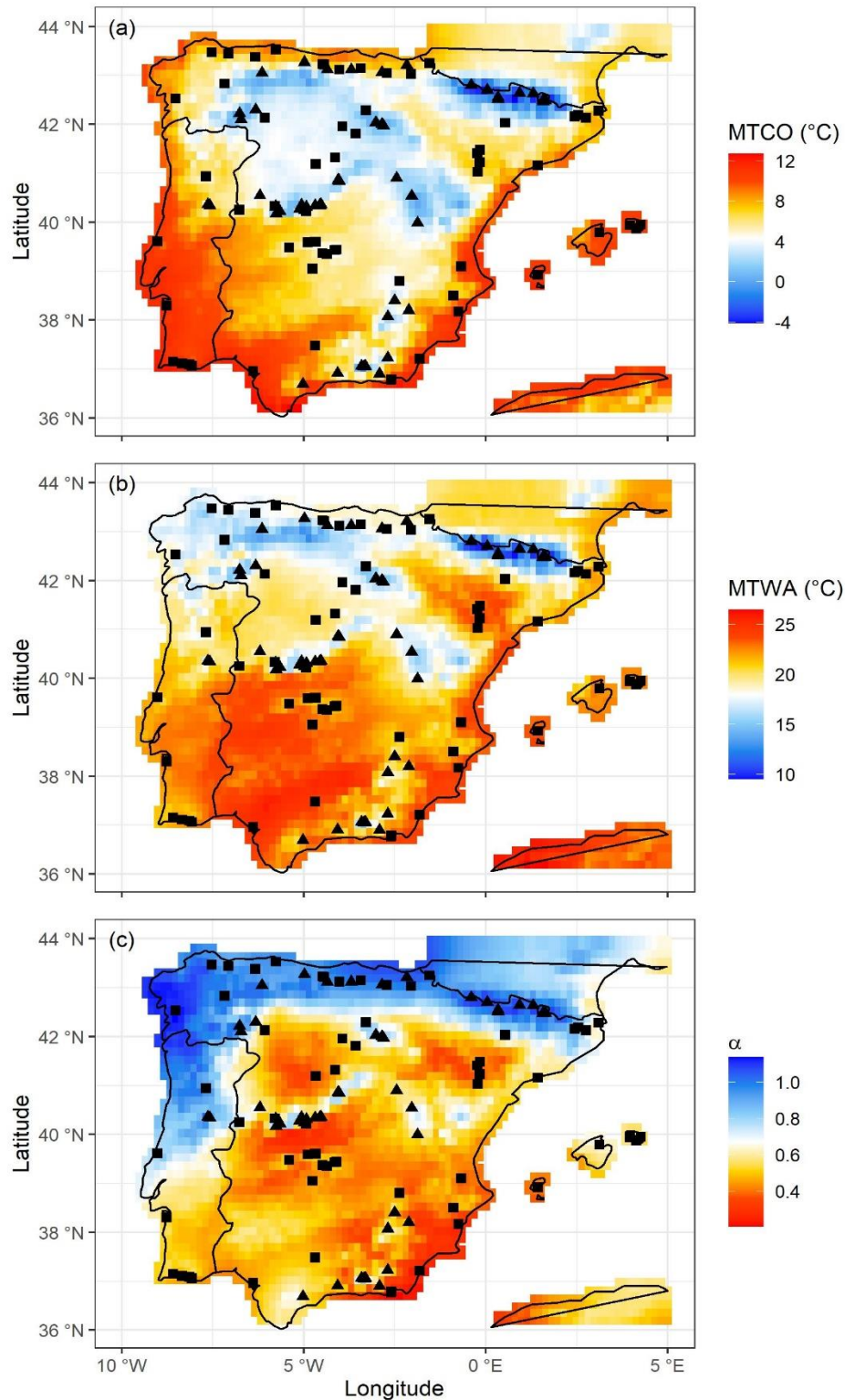
876 ~~Table 3~~Table 4. Assessment of the significance of anomalies to 0.5 ka through time with
877 latitude and elevation. The slope is obtained by linear regression of the anomaly onto the
878 longitude or elevation. p is the significance of the slope (bold parts: $p < 0.05$). x_0 is the point
879 where the anomaly is 0 in the linear equation, which indicates longitude or elevation where
880 the anomaly changes sign.

881 Figure 1. Climate space represented by mean temperature of the coldest month (MTCO),
882 mean temperature of the warmest month (MTWA), and plant-available moisture as
883 represented by α , an estimate of the ratio of actual evapotranspiration to equilibrium
884 evapotranspiration. The grey points show climate values for a rectangular area (21° W ~ 150°
885 E, 29° N ~ 82° N) enclosing the SMPDS data set, derived from the Climate Research Unit
886 CRU CL 2.0 database (New et al., 2002). The black points show climate values of the
887 SMPDS dataset. The red points show climate values of the Iberian Peninsula region in the
888 SMPDS dataset.
889



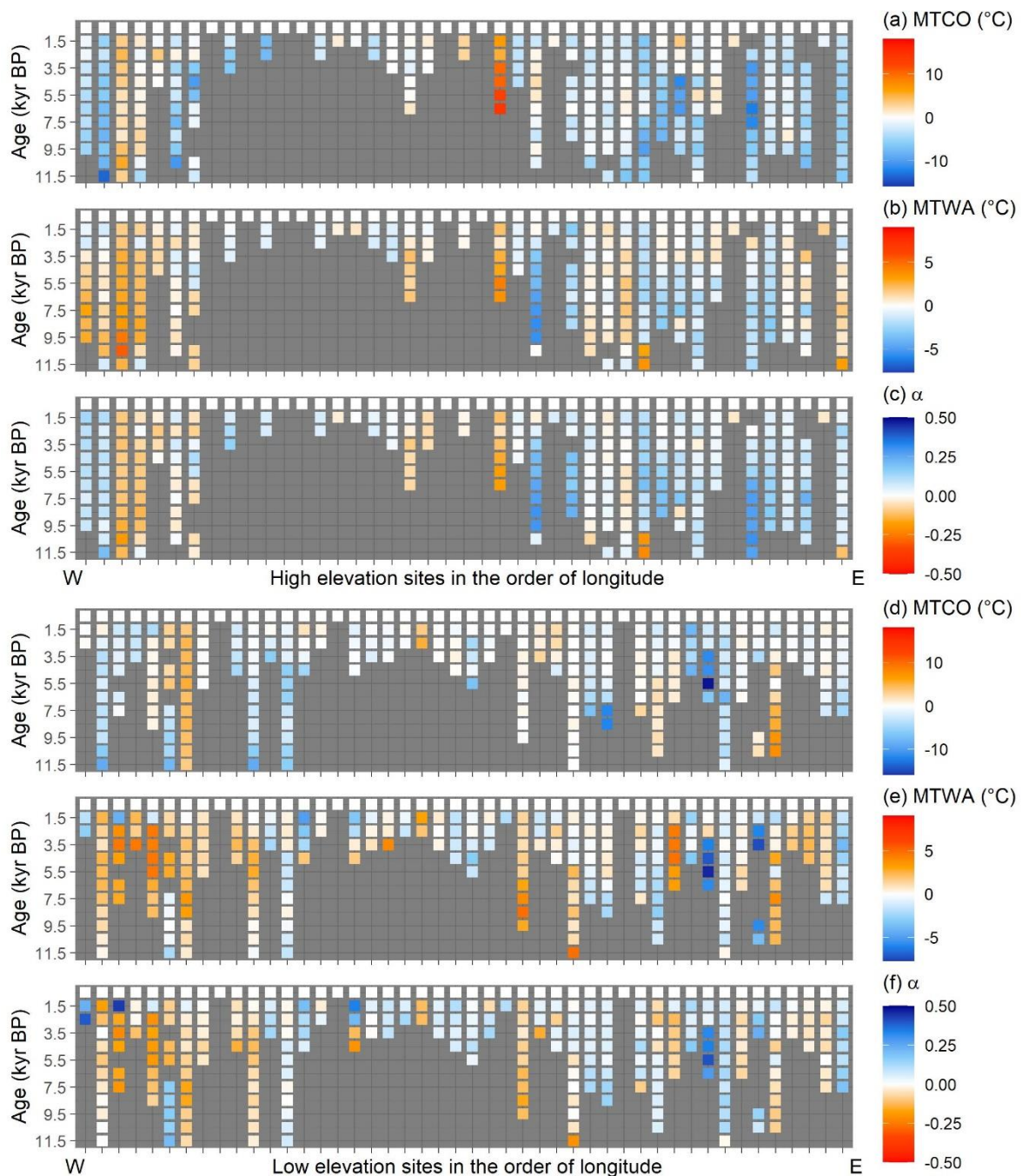
890

891 Figure 2. Map showing the location of the 117 fossil sites in the Iberian Peninsula used for
 892 climate reconstructions. Sites lower than 1000 m a.s.l. ~~m above sea level~~ are shown as
 893 squares, sites higher than 1000 m a.s.l. ~~m above sea level~~ are shown as triangles. The base
 894 maps show modern (a) mean temperature of the coldest month (MTCO), (b) mean
 895 temperature of the warmest month (MTWA), and (c) plant-available moisture as represented
 896 by α , an estimate of the ratio of actual evapotranspiration to equilibrium evapotranspiration.
 897



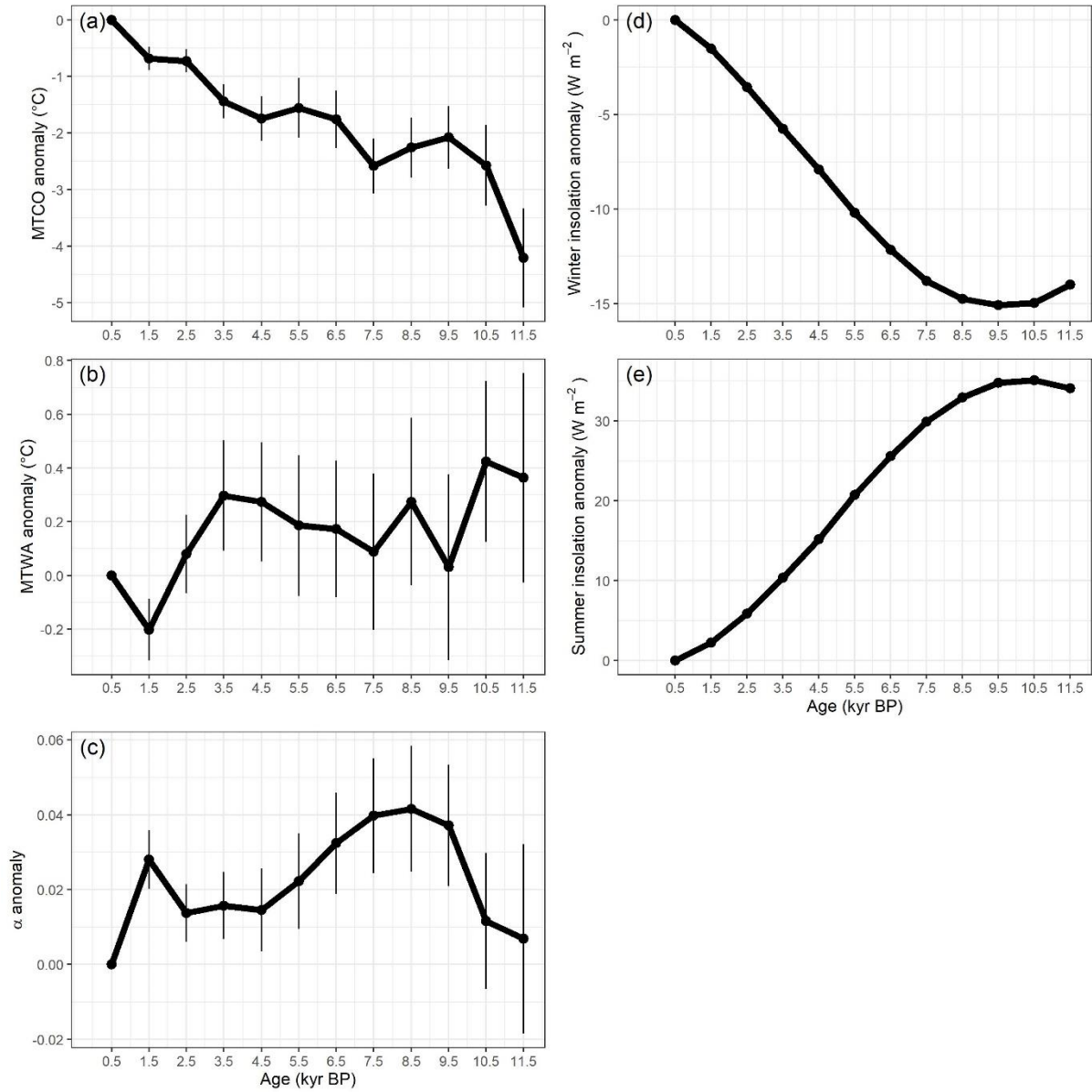
898

899 Figure 3. Reconstructed anomalies in climate at individual sites through time. The sites are
 900 grouped into high (>1000m) and low (<1000m) elevation sites and organised from west to
 901 east. Grey cells indicate periods or longitudes with no data. The individual plots show the
 902 anomalies in reconstructed (a,d) mean temperature of the coldest month (MTCO), (b,e) mean
 903 temperature of the warmest month (MTWA), and (c,f) plant-available moisture as
 904 represented by α , an estimate of the ratio of actual evapotranspiration to equilibrium
 905 evapotranspiration. The anomalies are expressed as deviations of the mean value in each bin
 906 (± 500 years) from the value at 0.5 ka at each site.
 907



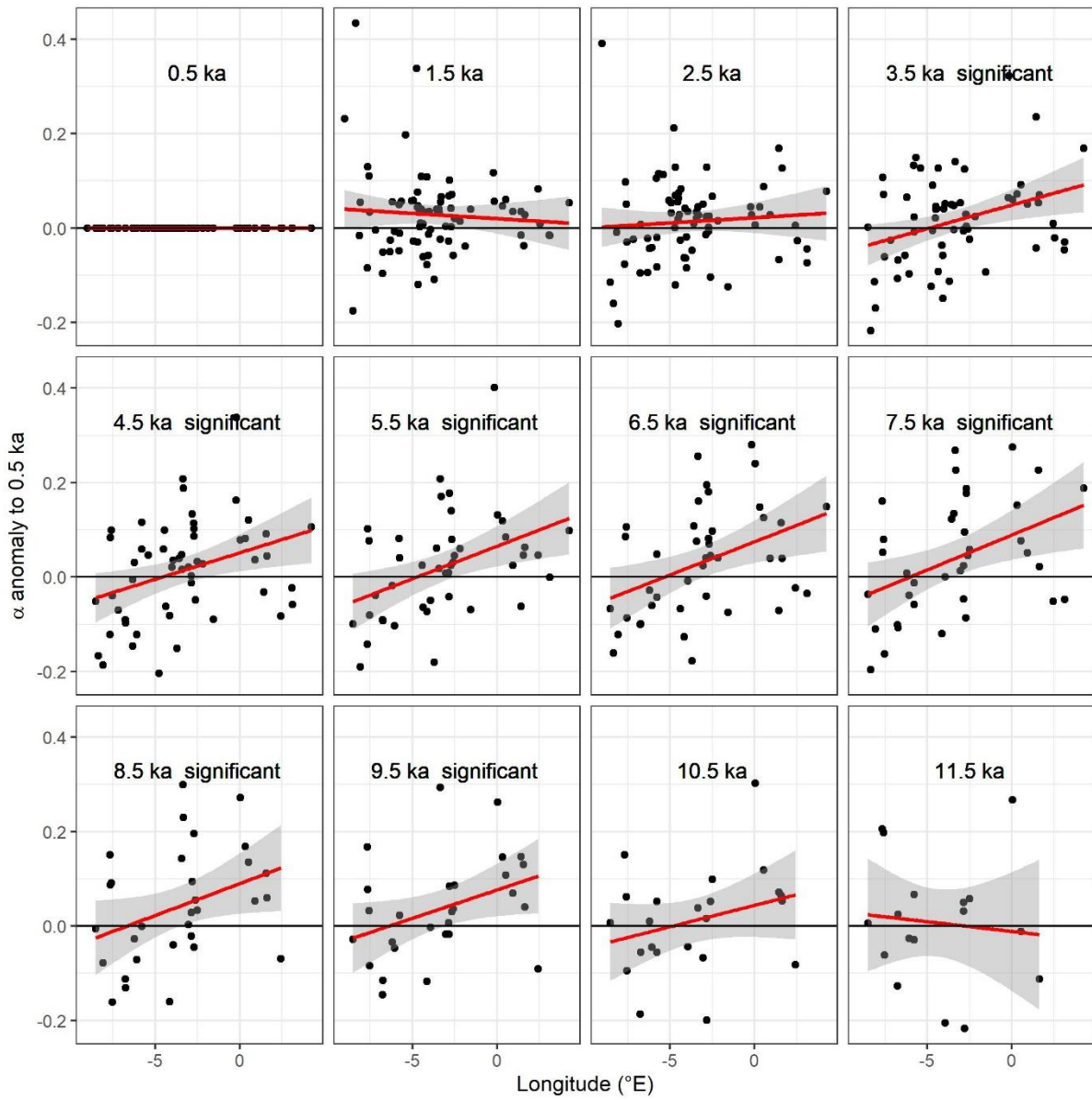
908

909 Figure 4. Reconstructed composite changes (anomalies to 0.5 ka) in (a) mean temperature of
 910 the coldest month (MTCO), (b) mean temperature of the warmest month (MTWA) and (c)
 911 plant-available moisture as represented by α , through the Holocene compared to changes in
 912 (d) winter and (e) summer insolation for the latitude of the Iberian Peninsula, using ± 500
 913 years as the bin. The black lines show mean values across sites, with vertical line segments
 914 showing the standard deviations of mean values using 1000 bootstrap cycles of site
 915 resampling.
 916



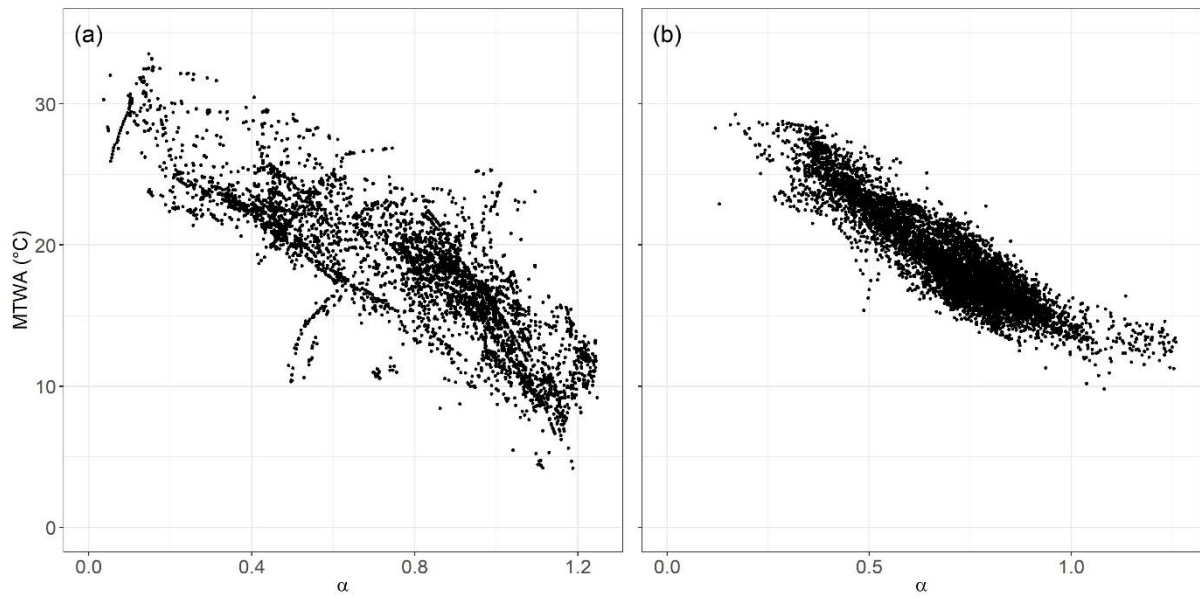
917

918 Figure 5. Changes in the west-east gradient of plant-available moisture as represented by
 919 anomalies in α relative to 0.5 ka at individual sites through the Holocene. The red lines show
 920 the regression lines. The shades indicate the 95 % confidence intervals of the regression lines.
 921



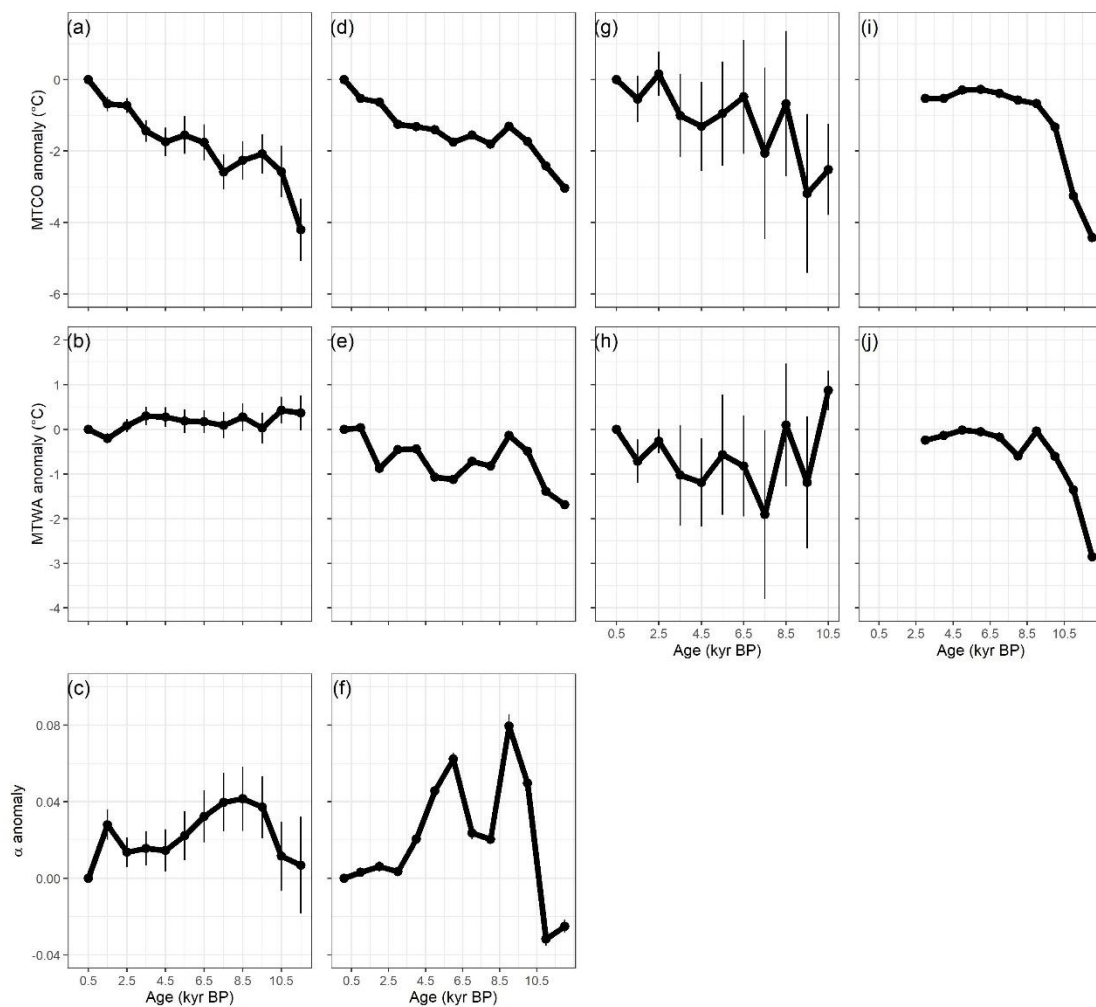
922

923 Figure 6. The relationship between mean temperature of the warmest month (MTWA) and
924 plant-available moisture as represented by α (a) in the modern climate data set, and (b) in the
925 Holocene reconstructions.
926



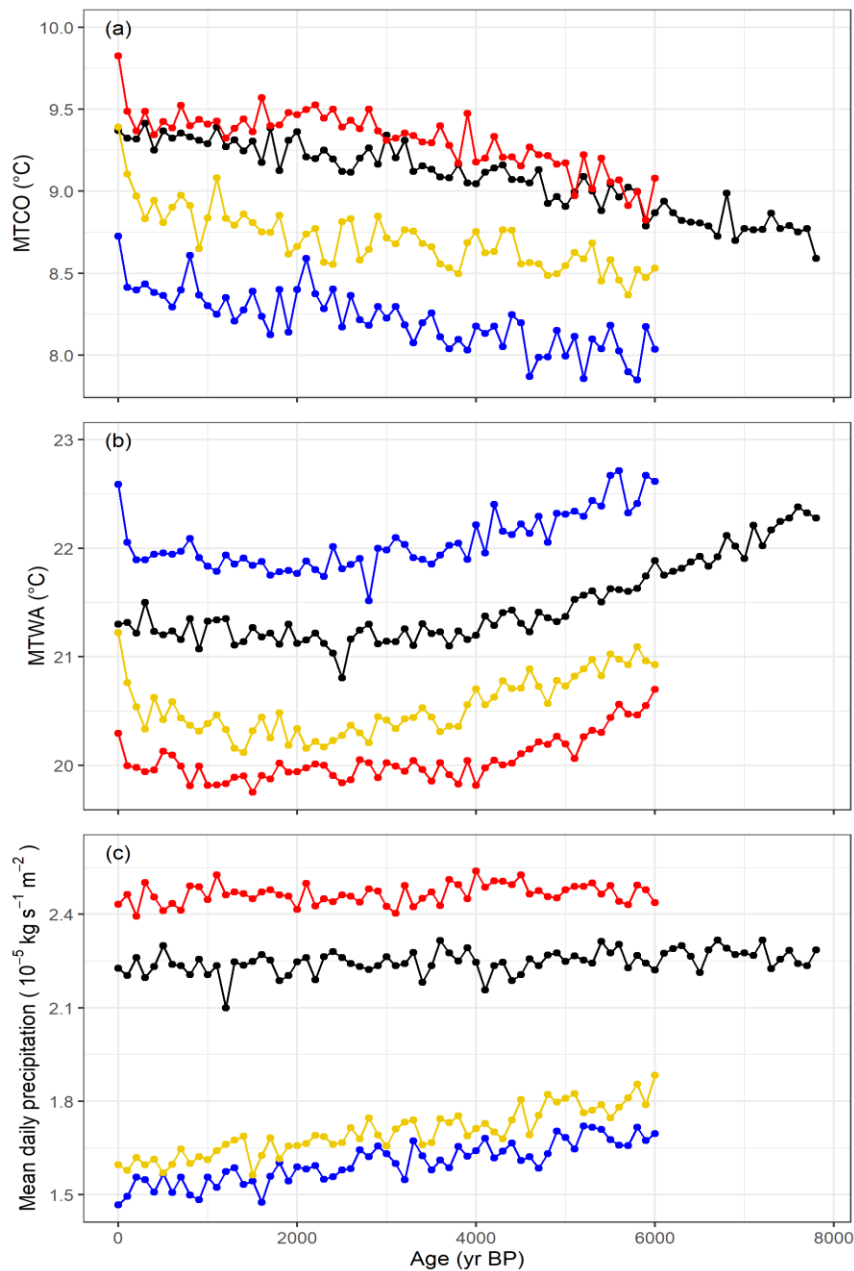
927
928
929

930 Figure 7. Comparison between reconstructed composite changes in climate anomalies. The first
 931 column represents this paper, the second column represents Mauri et al. (2015), the third
 932 column represents Kaufman et al. (2020), the fourth column represents Tarroso et al. (2016).
 933 The composite curves from this paper and Kaufman et al. (2020) are calculated from individual
 934 reconstructions, using anomalies to 0.5 ka and a bin of ± 500 years (time slices are 0.5, 1.5, ...,
 935 11.5 ka). The composite curves from Mauri et al. (2015) are converted directly from the gridded
 936 time slices which are provided with anomalies to 0.1 ka and a bin of ± 500 years (time slices
 937 are 1, 2, ..., 12 ka). The composite curves from Tarroso et al. (2016) are also converted directly
 938 from the gridded time slices provided, with anomalies to 0.5 ka and a bin of ± 500 years (time
 939 slices are 3, 4, ..., 12 ka). Note that Tarroso et al. (2016) applied a smoothing to the data such
 940 that the plots in the paper do not show the excursion in MTWA at 8 ka. In all of the plots, the
 941 black lines show mean values across sites, with vertical line bars showing the standard
 942 deviation of mean values using 1000 bootstrap cycles of site/grid resampling.
 943



944
 945

946 Figure 8. Simulated mean values of mean temperature of the coldest month (MTCO), mean
 947 temperature of the warmest month (MTWA) and mean daily precipitation in Iberian
 948 Peninsula between 8 ka and 0 ka, smoothed using 100 year bins. Here BP means before 1950
 949 AD. The black lines represent Max Planck Institute Earth System Model (MPI) simulations,
 950 the red lines represent Alfred Wagner Insitute Earth System Model (AWI) simulations, the
 951 blue lines represent Institut Pierre Simon Laplace Climate Model (IPSL-CM5) TR5AS
 952 simulations, the orange lines represent Institut Pierre Simon Laplace Climate Model (IPSL-
 953 CM6) TR6AV simulations. The four simulations were forced by evolving orbital parameters
 954 and greenhouse gas concentrations. The four models have different spatial resolution, with
 955 the finest resolution being $1.875^\circ \times 1.875^\circ$ (AWI, MPI) and the coarsest resolution being
 956 $1.875^\circ \times 3.75^\circ$ (IPSL-CM5, TR5AS).



957

958 Table 1. Details of the fossil pollen sites used. The fossil pollen data from the Iberian Peninsula were compiled by Shen et al. (2021) and obtained
 959 from <https://doi.org/10.17864/1947.000343>. The reference list of this table can be found in the supplementary.
 960

<u>site name</u>	<u>entity name</u>	<u>longitude (°E)</u>	<u>latitude (°N)</u>	<u>elevation (m)</u>	<u>earliest sample (yr BP)</u>	<u>latest sample (yr BP)</u>	<u>length of record (yr)</u>	<u>no of samples</u>	<u>no of dating points</u>	<u>source</u>	<u>reference</u>
Albufera Alcudia	ALCUDIA	3.12	39.79	0	7921	17	7904	54	4	EPD	Burjachs et al., (1994)
Algendar	ALGENDAR	3.96	39.94	21	8908	3816	5092	118	4	EPD	Yll et al., (1995, 1997)
Almenara de Adaja	ADAJA	-4.67	41.19	784	2830	477	2353	25	2	EPD	López Merino et al., (2009)
Alsa	ALSA	-4.02	43.12	560	4908	150	4758	24	3	EPD	Mariscal (1993)
Alvor Estuary Ribeira do Farelo Ribeira da Torre	Abi 05/07	-8.59	37.15	1	7840	1699	6141	76	9	author	Schneider et al., (2010, 2016)
Antas	ANTAS	-1.82	37.21	0	11141	4309	6832	95	6	EPD	Yll et al., (1995); Cano Villanueva, J. P. (1997); Pantaléon-Cano et al., (2003)
Arbarrain Mire	ARBARRAIN	-2.17	43.21	1004	6872	78	6794	91	8	author	Pérez-Díaz et al., (2018)
Armacao de Pera Ribeira de Alcantarilha	ADP 01/06	-8.34	37.11	2	7926	8	7918	17	7	author	Schneider et al., (2010, 2016)
Armena	Armena	0.34	42.51	2238	5668	2217	3451	53	27	author	Leunda et al., (2019)
Arroyo de Aguas Frias	AGUASFRIAS	-5.12	40.27	1120	196	-41	237	50	5	author	Julio Camarero et al., (2019)
Arroyo de las Cárcavas	CARCAVAS	-4.03	40.84	1300	2346	-57	2403	40	6	EPD	Morales-Molino et al., (2017a)
Arroyo de Navalacarreta	NAVALACA	-4.03	40.85	1250	706	-60	766	38	6	EPD	Morales-Molino et al., (2017a)
Arroyo de Valdeconejos	VALDECON	-4.06	40.86	1380	611	-56	667	44	8	EPD	Morales-Molino et al., (2017a)
Atxuri	ATXURI01	-1.55	43.25	500	6877	495	6382	33	2	EPD	Penalba (1994); Penalba and Garmendia (1989)
Ayoó de Vidriales	AYOO	-6.07	42.13	780	11846	-26	11872	63	15	EPD	Morales-Molino & García-Antón (2014)
Basa de la Mora	BSM08	0.33	42.55	1906	9856	184	9672	135	16	author	Pérez-Sanz et al., (2013)
Bassa Nera	BSN6	0.92	42.64	1891	9599	-55	9654	62	8	author	Garces-Pastor et al., (2017)
Bermu Mire	BERMU	-4.15	39.43	783	1192	-25	1217	38	8	author	Luelmo-Lautenschlaeger et al., (2018a)
Borreguil de la Caldera	BdIC-01	-3.32	37.05	2992	1440	-56	1496	80	6	author	Ramos-Román et al., (2016)

Bosc dels Estanyons	BOSCESTA	1.63	42.48	2180	11761	26	11735	91	8	EPD	Miras et al., (2007); De Beaulieu et al., (2005)
Botija Bog	BOTIJA	-4.7	39.6	755	3773	82	3691	25	4	author	Luelmo-Lautenschlaeger et al., (2018b)
Cañada de la Cruz	CANCRUZ	-2.69	38.07	1595	9413	-6	9419	39	14	EPD	Yll et al., (1997)
Cala'n Porter	CPORTER	4.13	39.87	24	8809	4802	4007	86	4	EPD	Yll et al., (1994, 1995)
Cala Galdana	GALDANA	3.96	39.94	47	8498	4830	3668	101	5	EPD	López-Merino et al., (2012)
Campo Lameiro	PRD4	-8.52	42.53	260	11948	-11	11959	42	6	EPD	Carrión et al., (2007)
Canada del Gitano Sierra de Baza	SBAZA	-2.7	37.23	1900	8460	103	8357	111	8	EPD	Cerrillo Cuenca et al., (2007); Cerrillo Cuenca & González Cordero (2011)
Canaleja	CANALEJA	-2.45	40.9	1029	11544	5515	6029	6	2	EPD	Carrion et al., (2001)
Castello Lagoon	Castello Lagoon core EM	3.1	42.28	2	4944	307	4637	85	10	author	Ejarque et al., (2016)
Cha das Lameiras	LAMEIRAS	-7.68	40.94	950	11982	539	11443	32	8	author	Burjachs & Expósito (2015)
Charco da Candieira	CANDIEIR	-7.58	40.34	1409	11970	32	11938	230	31	EPD	Mariscal Alvarez et al., (1983)
Creixell	CreixellIT	1.43	41.16	1	6438	723	5715	32	2	EPD	López-Sáez et al., (2013)
Cueto de la Avellanosa	CUETOAV	-4.36	43.12	1320	6969	292	6677	34	3	EPD	López-Sáez et al., (2017)
Culazón	CULAZON	-4.49	43.23	592	3895	-44	3939	69	11	EPD	van der Knaap & van Leeuwen (1984, 1995, 1997)
El Brezosa	BREZOSA	-4.36	39.35	733	3958	-16	3974	68	11	author	Burjachs & Expósito (2015); Burjachs et al., (1997)
El Carrizal	CARRIZAL	-4.14	41.32	860	9851	0	9851	50	6	EPD	Morales-Molino et al., (2018)
El Maíllo mire	MAI	-6.21	40.55	1100	10687	91	10596	104	10	EPD	Franco-Múgica, et al., (2005)
El Payo	ELPAYO	-6.77	40.25	1000	571	-56	627	50	6	EPD	Morales-Molino et al., (2013)
El Perro mire	ELPERRO	-4.76	39.05	690	4694	-69	4763	41	10	author	Abel Schaad et al., (2009); Silva-Sánchez et al., (2016)
El Portalet	PORTALET	-0.4	42.8	1802	11838	2128	9710	207	13	author	Luelmo-Lautenschlaeger (2019a, 2019b)
El Redondo	REDONDO	-5.66	40.22	1765	3222	31	3191	60	4	author	González-Sampéris et al., (2006)
El Sabinar	SABINAR	-2.12	38.2	1117	6580	1140	5440	129	9	EPD	López-Sáez et al., (2016)
El Tiemblo	TIEMBLO	-4.53	40.36	1250	3184	3	3181	60	9	author	Carrión et al., (2004)
Elx	ELX	-0.75	38.17	1	9903	3392	6511	79	4	EPD	López-Sáez et al., (2018a)

Enol	ENOL	-4.99	43.27	1075	10910	2487	8423	30	7	author	Moreno et al., (2011)
Es Grau	ESGRAU	4.26	39.95	2	7648	-13	7661	98	15	EPD	Buriachs et al., (2017)
Espinosa de Cerrato	CERRATO	-3.94	41.96	885	11578	822	10756	157	7	author	Múgica et al., (2001); Morales-Molino et al., (2017b)
Estanilles	ESTANILLES	1.3	42.63	2247	11908	7646	4262	57	11	EPD	Pérez-Obiol et al., (2012)
Estanya	Estanya Catena	0.53	42.03	677	11882	-37	11919	48	21	author	González-Sampérez et al., (2017); Morellón et al., (2011)
Fuente de la Leche	LECHE	-5.06	40.35	1382	2783	-18	2801	58	10	author	Robles-López et al., (2018)
Fuente del Pino Blanco	PINOBLANCO	-4.98	40.24	1343	653	-38	691	96	5	author	Robles-López et al., (2018)
Hinojos Marsh	HINOJOS	-6.39	36.96	2	4737	2682	2055	46	5	author	López-Sáez et al., (2018b)
Hort Timoner	HTIMONER	4.13	39.88	40	8686	5089	3597	46	4	EPD	Yll et al., (1997)
Hoya del Castillo	N-CAS	-0.16	41.48	258	10740	5629	5111	34	3	EPD	Davis & Stevenson (2007)
La Cruz	LACRUZ	-1.87	39.99	1024	1521	12	1509	23	2	EPD	Buriachs (1996)
La Molina mire	MOLINAE	-6.33	43.38	650	4482	388	4094	152	6	author	López-Merino et al., (2011)
Labradillos Mire	LABRADILLOS	-4.57	40.34	1460	1447	184	1263	25	5	author	Robles López et al., (2017)
Lago de Ajo	LAGOAJO	-6.15	43.05	1570	11755	2175	9580	44	6	EPD	McKeever et al., (1984); Allen et al., (1996)
Lagoa Comprida 2	LAGOA_CO	-7.64	40.36	1650	9863	94	9769	68	4	EPD	Janssen & Woldringh (1981); Moe & Van Der Knaap (1990); Van Den Brink & Janssen (1985)
Lagoa Travessa	TRAVESS1	-8.77	38.3	3	8174	3617	4557	65	4	EPD	Mateus (1985); Mateus (1989)
Laguna de la Mosca	LdlMo composite	-3.31	37.06	2889	8344	-63	8407	68	18	author	Manzano et al., (2019)
Laguna de la Mula	LdlM 10-02	-3.42	37.06	2497	4581	-60	4641	32	8	author	Jiménez-Moreno et al., (2013)
Laguna de la Roya	LAROYA	-6.77	42.22	1608	11927	-41	11968	54	7	PANGAE A	Allen et al., (1996)
Laguna de Rio Seco	Laguna de Rio Seco core 1	-3.35	37.05	3020	10455	-54	10509	69	13	author	Anderson et al., (2011)
Laguna Guallar	N-GUA	-0.23	41.41	336	10654	8056	2598	30	6	EPD	Davis & Stevenson (2007)
Laguna Mesagosa	LAGMESAG	-2.81	41.97	1600	11981	-48	12029	90	5	EPD	Engelbrechten (1999)
Laguna Negra	LAGNEGRA	-2.85	42	1760	11253	-48	11301	68	9	EPD	Engelbrechten (1999)
Laguna Salada Chiprana	N-SAL	-0.17	41.23	150	6872	-40	6912	39	4	EPD	Valero-Garces et al., (2000)

Lake Banyoles	BANYOLES_1, Banyoles SB2	2.75	42.13	174	11952	3316	8636	141	15	EPD	Pèrez-Obiol & Julià (1994); Revelles et al., (2015)
Lake Saloio	SALOIO	-9.02	39.61	70	2804	313	2491	24	2	EPD	Gomes (2011)
Lanzahíta	LANZBOG	-4.94	40.22	558	2657	-51	2708	51	8	author	López-Sáez et al., (1999, 2010)
Las Animas Mire	ANIMAS	-5.03	36.69	1403	797	-57	854	48	10	author	Alba-Sánchez et al., (2019)
Las Lanchas	LANCHAS	-4.89	39.59	800	374	-8	382	20	2	author	Luelmo-Lautenschlaeger et al., (2018c)
Las Pardillas	LASPARDI	-3.03	42.03	1850	10954	404	10550	74	4	EPD	Goñi & Hannon (1999)
Las Vinuelas	VINUELAS	-4.49	39.37	761	4210	-56	4266	58	9	author	Morales-Molino et al., (2019)
Les Palanques	PALANQUES	2.44	42.16	460	10011	524	9487	77	3	EPD	Revelles et al., (2018)
Manaderos	Manaderos core	-4.69	40.34	1292	1293	37	1256	59	9	author	Robles-López et al., (2020)
Marbore	Marbore composite	0.04	42.7	2612	11683	-18	11701	61	18	author	Leunda et al., (2017)
Monte Areo mire	AREO	-5.77	43.53	200	11547	-35	11582	55	12	EPD	López-Merino et al., (2010)
Montes do Buio Cuadramón	CUAII	-7.53	43.47	700	11347	241	11106	19	4	EPD	González et al., (2000)
Navamuno	Navamuno S 3	-5.78	40.32	1505	11971	-28	11999	207	12	author	López-Sáez et al., (2020)
Navarrés	NAVA1, NAVARRE3	-0.68	39.1	225	11104	3131	7973	72	15	EPD	Carrion & Dupre (1996); Carrión & Van Geel (1999)
Ojos del Tremendal	Ojos del Tremendal core 1	-2.04	40.54	1650	11875	1253	10622	52	4	author	Stevenson (2000)
Patateros bog	PATATERO	-4.67	39.6	700	2655	-19	2674	28	4	EPD	Dorado-Valiño et al., (2014)
Peña Negra	PENANEGR	-5.79	40.33	1000	3434	-62	3496	63	7	EPD	Stefanini (2008)
Pedrido	PEDRIDO	-7.07	43.44	770	5256	106	5150	71	30	EPD	Mighall et al., (2006)
Pena de Cadela	CADELA	-7.17	42.83	970	5233	-14	5247	91	9	EPD	Abel-Schaad & López-Sáez (2013)
Pico del Sertal	SERTAL	-4.44	43.22	940	5200	106	5094	9	3	EPD	Mariscal Alvarez (1986)
Pla de l'Estany	PLAESTANY	2.54	42.19	520	3577	-37	3614	43	4	EPD	Burjachs (1994)
Planell de Perafita	PERAFITA	1.57	42.48	2240	10244	-1	10245	56	11	EPD	Miras et al., (2010)
Posidonia Lligat	LLIGAT	-3.29	42.29	-3	779	15	764	32	5	EPD	López-Sáez et al., (2009)
Pozo de la Nieve	PozoN 2015 core	-4.55	40.35	1600	2258	-37	2295	41	10	author	Robles-López et al., (2017)

Praillos de Bossier Mire	BOSSIER	-4.07	36.91	1610	3428	4	3424	25	3	EPD	Abel-Schaad et al., (2017)
Prat de Vila	PRATVILA	1.43	38.92	4	10776	538	10238	29	5	EPD	Burjachs et al., (2017)
Puerto de Belate	BELATE01	-2.05	43.03	847	8457	1746	6711	60	3	EPD	Penalba (1994); Penalba and Garmendia (1989)
Puerto de las Estacas de Trueba	ESTACAS	-3.7	43.12	1160	6263	391	5872	9	3	PANGAE A	Mariscal (1989)
Puerto de Los Tornos	TORNOS01	-3.43	43.15	920	8718	-34	8752	47	4	EPD	Penalba and Garmendia (1989)
Puerto de Serranillos	SERRANIL	-4.93	40.31	1700	2254	-50	2304	34	5	EPD	López-Merino et al., (2009)
Quintanar de la Sierra	QUINTA02	-3.02	42.03	1470	11995	1953	10042	37	20	EPD	Penalba (1994); Penalba and Garmendia (1989)
Roquetas de Mar	ROQUETAS	-2.59	36.79	0	6910	1057	5853	32	3	EPD	Yll et al., (1995); Cano Villanueva (1997); Pantaléon-Cano (2003); Obiol (1994)
Salada Pequeña	N-PEQ	-0.22	41.03	357	4350	669	3681	43	5	EPD	Davis (2010)
Saldropo	SALDROPO	-2.72	43.05	625	7577	403	7174	76	3	EPD	Penalba (1994, 1989)
Salines playa-lake	SALINES	-0.89	38.5	475	11905	1394	10511	74	7	EPD	Burjachs et al., (2017)
San Rafael	SANRAFA	-2.6	36.77	0	10846	-30	10876	134	6	EPD	Cano Villanueva (1997); Pantaléon-Cano et al., (2003); Yll et al., (1995)
Sanabria Marsh	SANABRIA	-6.73	42.1	1050	11832	0	11832	79	9	EPD	Allen et al., (1996); Hannon (1985); Turner & Hannon (1988)
Serra Mitjana Fen	MITJANA	1.58	42.47	2406	1490	412	1078	15	2	EPD	Miras et al., (2015)
Serrania de las Villuercas	VILLUERCAS	-5.4	39.48	1000	4156	128	4028	31	4	author	Gil-Romera et al., (2008)
Sierra de Gádor	GADOR	-2.92	36.9	1530	6222	1195	5027	86	6	EPD	Carrión et al., (2003)
Siles Lake	SILES	-2.5	38.4	1320	11527	189	11338	67	12	EPD	Carrión (2002)
Tubilla del Lago	TUB	-3.57	41.81	900	7436	31	7405	88	13	EPD	Morales-Molino et al., (2017b)
Turbera de La Panera Cabras	PANERA	-5.76	40.17	1648	164	-56	220	23	2	EPD	Abel Schaad et al., (2009)
Valdeyernos bog	VALDEYER	-4.1	39.44	850	3160	-60	3220	25	4	EPD	Dorado-Valiño et al., (2014)
Valle do Lobo Ribeira de Carcavai	VdL PB2	-8.07	37.06	2	8331	16	8315	144	20	author	Schneider et al., (2010, 2016)
Verdeospesoa mire	VERDEOSPES OA	-2.86	43.06	1015	11137	0	11137	91	12	author	Pérez-Díaz & López-Sáez (2017)

<u>Vilamora Ribeira de Quarteira</u>	<u>Vilamora P01-5</u>	<u>-8.14</u>	<u>37.09</u>	<u>4</u>	<u>3851</u>	<u>919</u>	<u>2932</u>	<u>30</u>	<u>12</u>	<u>author</u>	<u>Schneider et al., (2010, 2016)</u>
<u>Villaverde</u>	<u>VILLAVERDE</u>	<u>-2.37</u>	<u>38.8</u>	<u>870</u>	<u>8066</u>	<u>0</u>	<u>8066</u>	<u>104</u>	<u>9</u>	<u>EPD</u>	<u>Carrión et al., (2001)</u>
<u>Xan de Llamas</u>	<u>XL</u>	<u>-6.32</u>	<u>42.3</u>	<u>1500</u>	<u>4113</u>	<u>34</u>	<u>4079</u>	<u>33</u>	<u>4</u>	<u>EPD</u>	<u>Morales-Molino et al., (2011)</u>
<u>Zoñar</u>	<u>ZONARcombi ned</u>	<u>-4.69</u>	<u>37.48</u>	<u>300</u>	<u>3234</u>	<u>-45</u>	<u>3279</u>	<u>52</u>	<u>17</u>	<u>author</u>	<u>Martín-Puertas et al., (2008)</u>

962 Table 42. Leave-out cross-validation (with geographically and climatically close sites
 963 removed) fitness of the modified version of fxTWA-PLS, for mean temperature of the coldest
 964 month (MTCO), mean temperature of the warmest month (MTWA) and plant-available
 965 moisture (α), with p-spline smoothed fx estimation, using bins of 0.02, 0.02 and 0.002,
 966 showing results for all the components. RMSEP is the root-mean-square error of prediction.
 967 Δ RMSEP is the per cent change of RMSEP using the current number of components than
 968 using one component less. p assesses whether using the current number of components is
 969 significantly different from using one component less, which is used to choose the last
 970 significant number of components (indicated in bold) to avoid over-fitting. The degree of
 971 overall compression is assessed by linear regression of the cross-validated reconstructions
 972 onto the climate variable, b_1 , $b_1.se$ are the slope and the standard error of the slope,
 973 respectively. The closer the slope (b_1) is to 1, the less the overall compression is.
 974
 975

	ncomp	R^2	avg. bias	max. bias	min. bias	RMSEP	Δ RMSEP	p	b_1	$b_1.se$
MTCO	1	0.70	-0.86	25.23	0.00	5.20	-39.97	0.001	0.89	0.01
	2	0.73	-0.73	25.00	0.00	4.87	-6.29	0.001	0.91	0.01
	3	0.74	-0.71	24.38	0.00	4.86	-0.32	0.001	0.91	0.01
	4	0.75	-0.59	24.27	0.00	4.70	-3.26	0.001	0.91	0.01
	5	0.74	-0.63	34.54	0.00	4.77	1.51	1.000	0.91	0.01
MTWA	1	0.52	-0.29	17.13	0.00	3.72	-26.88	0.001	0.69	0.01
	2	0.56	-0.14	17.20	0.00	3.53	-5.06	0.001	0.71	0.01
	3	0.56	-0.13	17.01	0.00	3.53	-0.20	0.008	0.71	0.01
	4	0.57	-0.11	17.30	0.00	3.47	-1.56	0.001	0.71	0.01
	5	0.57	-0.11	17.34	0.00	3.48	0.10	0.780	0.71	0.01
α	1	0.65	-0.014	0.787	0.000	0.165	-39.59	0.001	0.76	0.01
	2	0.68	-0.016	0.781	0.000	0.159	-3.55	0.001	0.77	0.01
	3	0.68	-0.017	0.757	0.000	0.158	-0.61	0.023	0.78	0.01
	4	0.69	-0.017	0.784	0.000	0.158	-0.43	0.108	0.79	0.01
	5	0.69	-0.017	0.850	0.000	0.158	0.26	0.985	0.80	0.01

976

977 Table 23. Canonical Correspondence Analysis (CCA) result of modern and fossil-
 978 reconstructed MTCO, MTWA and α . The summary statistics for the ANOVA-like
 979 permutation test (999 permutations) are also shown. VIF is the variance inflation factor, Df is
 980 the number of degrees of freedom, χ^2 is the constrained eigenvalue (or the sum of constrained
 981 eigenvalues for the whole model), F is significance, and Pr (>F) is the probability. [The CCA](#)
 982 [plots can be found in the Supplementary \(Fig. S11\).](#)
 983

Modern	Axes	Axis 1	Axis 2	Axis 3	VIF
	Constrained eigenvalues	0.3819	0.1623	0.1087	/
	Correlations of the environmental variables with the axes:				
	MTCO	-0.815	0.579	0.012	1.31
	MTWA	-0.700	-0.203	0.685	3.34
	α	0.883	0.430	-0.187	3.39
		Df	χ^2	F	Pr (>F)
	Whole model	3	0.6530	78.113	0.001
	MTCO	1	0.3082	110.597	0.001
	MTWA	1	0.1602	57.489	0.001
	α	1	0.1846	66.252	0.001
	CCA 1	1	0.3819	137.076	0.001
	CCA 2	1	0.1623	58.252	0.001
	CCA 3	1	0.1087	39.011	0.001
Fossil-reconstructed	Axes	Axis 1	Axis 2	Axis 3	VIF
	Constrained eigenvalues	0.3601	0.2266	0.2037	/
	Correlations of the environmental variables with the axes:				
	MTCO	0.430	0.776	0.462	1.34
	MTWA	0.987	0.141	-0.076	5.40
	α	-0.947	0.088	-0.308	5.28
		Df	χ^2	F	Pr (>F)
	Whole model	3	0.7905	226.98	0.001
	MTCO	1	0.2465	212.34	0.001
	MTWA	1	0.3298	284.07	0.001
	α	1	0.2142	184.53	0.001
	CCA 1	1	0.3601	310.19	0.001
	CCA 2	1	0.2266	195.24	0.001
	CCA 3	1	0.2037	175.51	0.001

985 Table 34. Assessment of the significance of anomalies to 0.5 ka through time with latitude
 986 and elevation. The slope is obtained by linear regression of the anomaly onto the longitude or
 987 elevation. p is the significance of the slope (bold parts: $p < 0.05$). x_0 is the point where the
 988 anomaly is 0 in the linear equation, which indicates longitude or elevation where the anomaly
 989 changes sign.
 990

		Longitude (°E)			Elevation (km)		
	age (ka)	slope	p	x_0	slope	p	x_0
MTCO (°C)	0.5	0.00	/	/	0.00	/	/
	1.5	-0.07	0.411	-13.02	-0.30	0.411	-1.21
	2.5	-0.15	0.095	-8.56	-0.52	0.179	-0.40
	3.5	-0.13	0.314	-14.83	-0.81	0.142	-0.77
	4.5	-0.12	0.444	-17.28	-0.69	0.319	-1.46
	5.5	-0.24	0.247	-9.49	-0.61	0.503	-1.43
	6.5	-0.18	0.372	-12.74	-0.87	0.293	-0.88
	7.5	-0.15	0.421	-20.39	-1.38	0.080	-0.67
	8.5	-0.03	0.890	-77.87	-1.58	0.065	-0.10
	9.5	0.01	0.954	156.31	-1.79	0.060	0.11
	10.5	0.20	0.474	9.25	-1.38	0.241	-0.64
	11.5	0.23	0.528	13.77	0.12	0.947	36.35
MTWA (°C)	0.5	0.00	/	/	0.00	/	/
	1.5	-0.01	0.862	-26.38	-0.05	0.830	-3.35
	2.5	-0.09	0.137	-2.80	-0.45	0.092	1.19
	3.5	-0.23	0.005	-2.03	-0.40	0.284	1.74
	4.5	-0.21	0.016	-2.01	-0.58	0.126	1.55
	5.5	-0.26	0.011	-2.43	-0.49	0.280	1.53
	6.5	-0.24	0.017	-2.30	-0.62	0.137	1.41
	7.5	-0.26	0.012	-3.02	-1.05	0.019	1.28
	8.5	-0.24	0.061	-2.43	-1.15	0.023	1.57
	9.5	-0.32	0.013	-3.20	-0.44	0.459	1.34
	10.5	-0.18	0.115	-1.23	0.54	0.276	0.44
	11.5	0.13	0.453	-7.25	0.37	0.663	0.22
α	0.5	0.00	/	/	0.00	/	/
	1.5	0.00	0.508	8.99	-0.01	0.393	3.40
	2.5	0.00	0.517	-9.89	0.02	0.249	0.19
	3.5	0.01	0.006	-4.91	0.02	0.191	0.28
	4.5	0.01	0.010	-4.60	0.05	0.008	0.79
	5.5	0.01	0.005	-4.75	0.05	0.027	0.67
	6.5	0.01	0.007	-5.34	0.06	0.004	0.60
	7.5	0.02	0.009	-6.05	0.09	0.000	0.75
	8.5	0.01	0.049	-6.67	0.09	0.000	0.88
	9.5	0.01	0.048	-6.40	0.07	0.012	0.70
	10.5	0.01	0.183	-4.85	0.02	0.535	0.59
	11.5	0.00	0.713	-2.76	0.03	0.654	0.93

992 **Appendix A**993 **Theoretical basis:**994 **The previous version of fxTWA-PLS (fxTWA-PLS1):**

995 The estimated optimum (\hat{u}_k) and unbiased tolerance (\hat{t}_k) of each taxon are calculated from
 996 the modern training data set as follows:

$$997 \quad \hat{u}_k = \frac{\sum_{i=1}^n y_{ik} x_i}{\sum_{i=1}^n y_{ik}} \quad (A1)$$

$$998 \quad \hat{t}_k = \sqrt{\frac{\sum_{i=1}^n y_{ik} (x_i - \hat{u}_k)^2}{(1 - 1/N_{2k}) \sum_{i=1}^n y_{ik}}} \quad (A2)$$

999 where

$$1000 \quad N_{2k} = \frac{1}{\sum_{i=1}^n \left(\frac{y_{ik}}{\sum_{i'=1}^n y_{i'k}} \right)^2} \quad (A3)$$

1001 where n is the total number of sites; y_{ik} is the observed abundance of the k^{th} taxon at the i^{th}
 1002 site; x_i is the observed climate value at the i^{th} site; N_{2k} is the effective number of occurrences
 1003 for the k^{th} taxon.

1004 fx correction is applied as weight in the form of $1/fx^2$ at regression at step 7 in Table 1 in Liu
 1005 et al. (2020). The regression step uses robust linear model fitting by the R code:

$$1006 \quad rlm(x_i \sim comp_1 + comp_2 + \dots + comp_{pls}, weights = 1/fx^2) \quad (A4)$$

1009 **The modified version of fxTWA-PLS (fxTWA-PLS2):**

1010 The distribution of y_{ik} is influenced by the distribution of the climate variable, so we need to
 1011 apply the fx correction when calculating optimum and tolerance for each taxon as follows:

$$1012 \quad \hat{u}_k = \frac{\sum_{i=1}^n \frac{y_{ik} x_i}{f_{x_i}}}{\sum_{i=1}^n \frac{y_{ik}}{f_{x_i}}} \quad (A5)$$

$$1013 \quad \hat{t}_k = \sqrt{\frac{\sum_{i=1}^n \frac{y_{ik} (x_i - \hat{u}_k)^2}{f_{x_i}}}{\left(1 - \frac{1}{N_{2k}}\right) \sum_{i=1}^n \frac{y_{ik}}{f_{x_i}}}} \quad (A6)$$

1014 where

$$1015 \quad N_{2k} = \frac{1}{\sum_{i=1}^n \left(\frac{\frac{y_{ik}}{f_{x_i}}}{\sum_{i'=1}^n \frac{y_{i'k}}{f_{x_{i'}}}} \right)^2} \quad (A7)$$

1016 The modified version of fxTWA-PLS applies fx correction separately at taxon calculation
 1017 and regression (step 2 and 7 in Table 1 in Liu et al., 2020), both using weight in the form of
 1018 $1/fx$. The regression step (step 7) then becomes:

$$1019 \quad rlm(x_i \sim comp_1 + comp_2 + \dots + comp_{pls}, weights = 1/fx) \quad (A8)$$

1020 The previous version uses fx values extracted from histograms, and different bin widths may
1021 result in different training results. The modified version applies P-splines histogram
1022 smoothing (Eilers and Marx, 2021) with third order difference penalty, which makes the fx
1023 values almost independent on the bin width. The optimal smoothing parameter of the P-spline
1024 penalty was determined by the HFS (Harville-Fellner-Schall) algorithm (Eilers and Marx,
1025 2021) for the Poisson likelihood for the histogram counts.

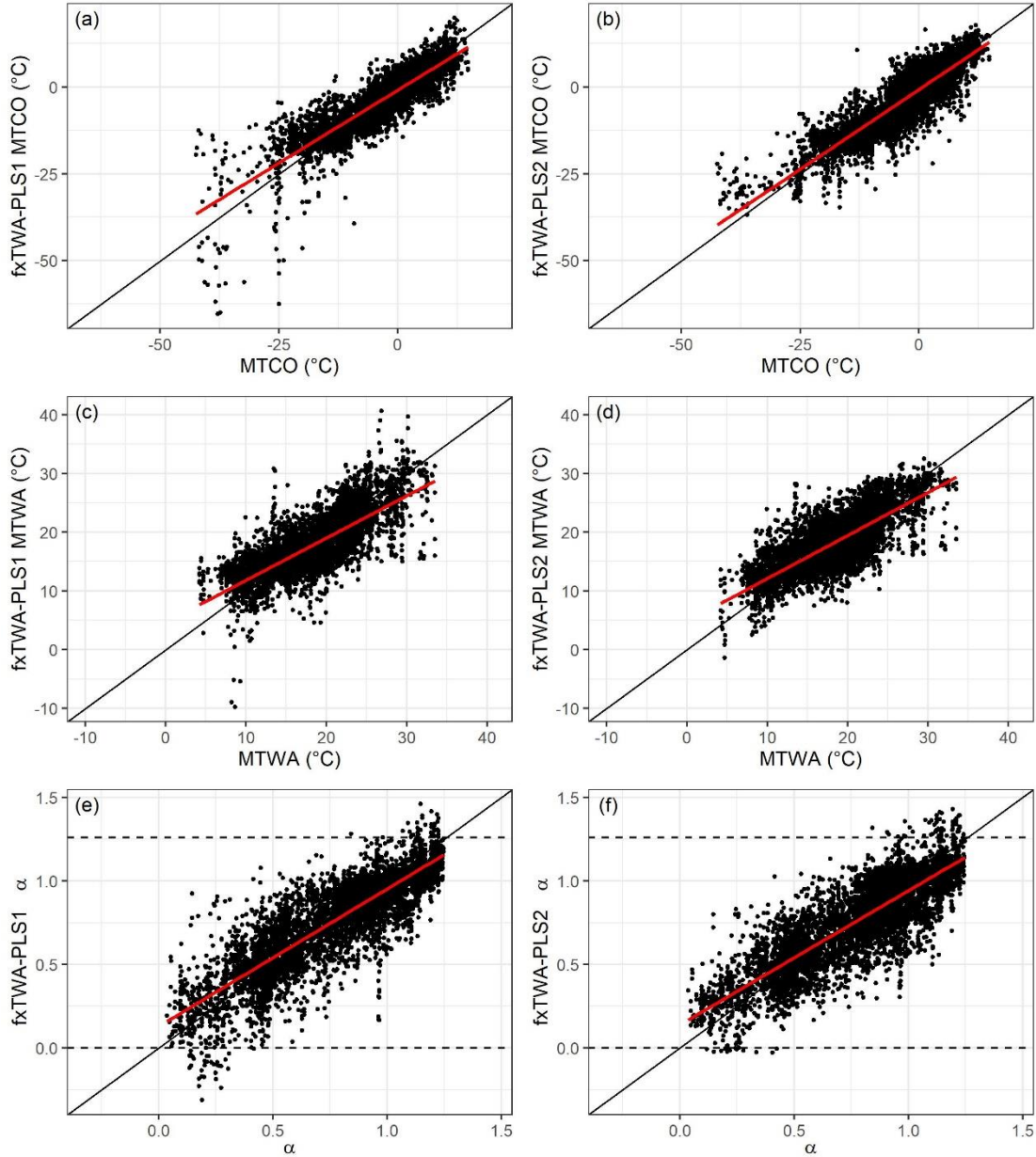
1026 Table A1. Leave-out cross-validation (with geographically and climatically close sites removed)
 1027 fitness of the previous and modified version of fxTWA-PLS (fxTWA-PLS1 and fxTWA-PLS2,
 1028 respectively), for mean temperature of the coldest month (MTCO), mean temperature of the warmest
 1029 month (MTWA) and plant-available moisture (α), using bins of 0.02, 0.02 and 0.002, respectively. n
 1030 is the number of components used. RMSEP is the root mean square error of prediction. Δ RMSEP is
 1031 the per cent change of RMSEP using the current number of components than using one component
 1032 less. p assesses whether using the current number of components is significantly different from using
 1033 one component less, which is used to choose the last significant number of components (indicated in
 1034 bold) to avoid overfitting. The degree of overall compression is assessed by doing linear regression to
 1035 the cross-validation result and the climate variable. b_1 , $b_1.se$ are the slope and the standard error of
 1036 the slope, respectively. The closer the slope (b_1) is to 1, the lower the overall compression is. fx
 1037 correction is set intrinsic in functions in `fxTWA` package for both versions in this paper, instead
 1038 of relying on an outside input in Liu et al. (2020), so the values of fxTWA-PLS1 might be slighted
 1039 different from values in [Table 2](#) [Table 3](#) in Liu et al. (2020), but it doesn't affect the conclusion.
 1040

	Method	n	R^2	avg. bias	max. bias	min. bias	RMSEP	Δ RMSEP	p	b_1	$b_1.se$
MTCO	fxTWA-PLS1	1	0.66	-0.86	31.17	0.00	5.21	-39.87	0.001	0.76	0.01
		2	0.72	-0.52	36.65	0.00	4.70	-9.78	0.001	0.80	0.01
		3	0.73	-0.47	41.18	0.00	4.62	-1.63	0.001	0.82	0.01
		4	0.73	-0.51	44.86	0.00	4.58	-1.01	0.006	0.82	0.01
		5	0.73	-0.41	58.35	0.00	4.62	0.89	0.708	0.83	0.01
	fxTWA-PLS2	1	0.70	-0.86	25.23	0.00	5.20	-39.97	0.001	0.89	0.01
		2	0.73	-0.73	25.00	0.00	4.87	-6.29	0.001	0.91	0.01
		3	0.74	-0.71	24.38	0.00	4.86	-0.32	0.001	0.91	0.01
		4	0.75	-0.59	24.27	0.00	4.70	-3.26	0.001	0.91	0.01
		5	0.74	-0.63	34.54	0.00	4.77	1.51	1.000	0.91	0.01
MTWA	fxTWA-PLS1	1	0.50	-0.53	17.91	0.00	3.87	-24.09	0.001	0.67	0.01
		2	0.56	-0.54	17.71	0.00	3.52	-8.98	0.001	0.69	0.01
		3	0.57	-0.49	25.14	0.00	3.52	0.09	0.565	0.73	0.01
		4	0.57	-0.43	34.92	0.00	3.56	1.12	0.974	0.75	0.01
		5	0.57	-0.46	32.23	0.00	3.55	-0.23	0.139	0.74	0.01
	fxTWA-PLS2	1	0.52	-0.29	17.13	0.00	3.72	-26.88	0.001	0.69	0.01
		2	0.56	-0.14	17.20	0.00	3.53	-5.06	0.001	0.71	0.01
		3	0.56	-0.13	17.01	0.00	3.53	-0.20	0.008	0.71	0.01
		4	0.57	-0.11	17.30	0.00	3.47	-1.56	0.001	0.71	0.01
		5	0.57	-0.11	17.34	0.00	3.48	0.10	0.780	0.71	0.01
α	fxTWA-PLS1	1	0.63	-0.020	0.773	0.000	0.174	-36.23	0.001	0.78	0.01
		2	0.69	-0.012	0.902	0.000	0.157	-9.66	0.001	0.79	0.01
		3	0.69	-0.011	0.820	0.000	0.155	-1.28	0.001	0.79	0.01
		4	0.70	-0.010	0.786	0.000	0.156	0.25	0.867	0.81	0.01
		5	0.70	-0.010	0.786	0.000	0.156	0.09	1.000	0.81	0.01
	fxTWA-PLS2	1	0.65	-0.014	0.787	0.000	0.165	-39.59	0.001	0.76	0.01
		2	0.68	-0.016	0.781	0.000	0.159	-3.55	0.001	0.77	0.01
		3	0.68	-0.017	0.757	0.000	0.158	-0.61	0.023	0.78	0.01
		4	0.69	-0.017	0.784	0.000	0.158	-0.43	0.108	0.79	0.01
		5	0.69	-0.017	0.850	0.000	0.158	0.26	0.985	0.80	0.01

1041

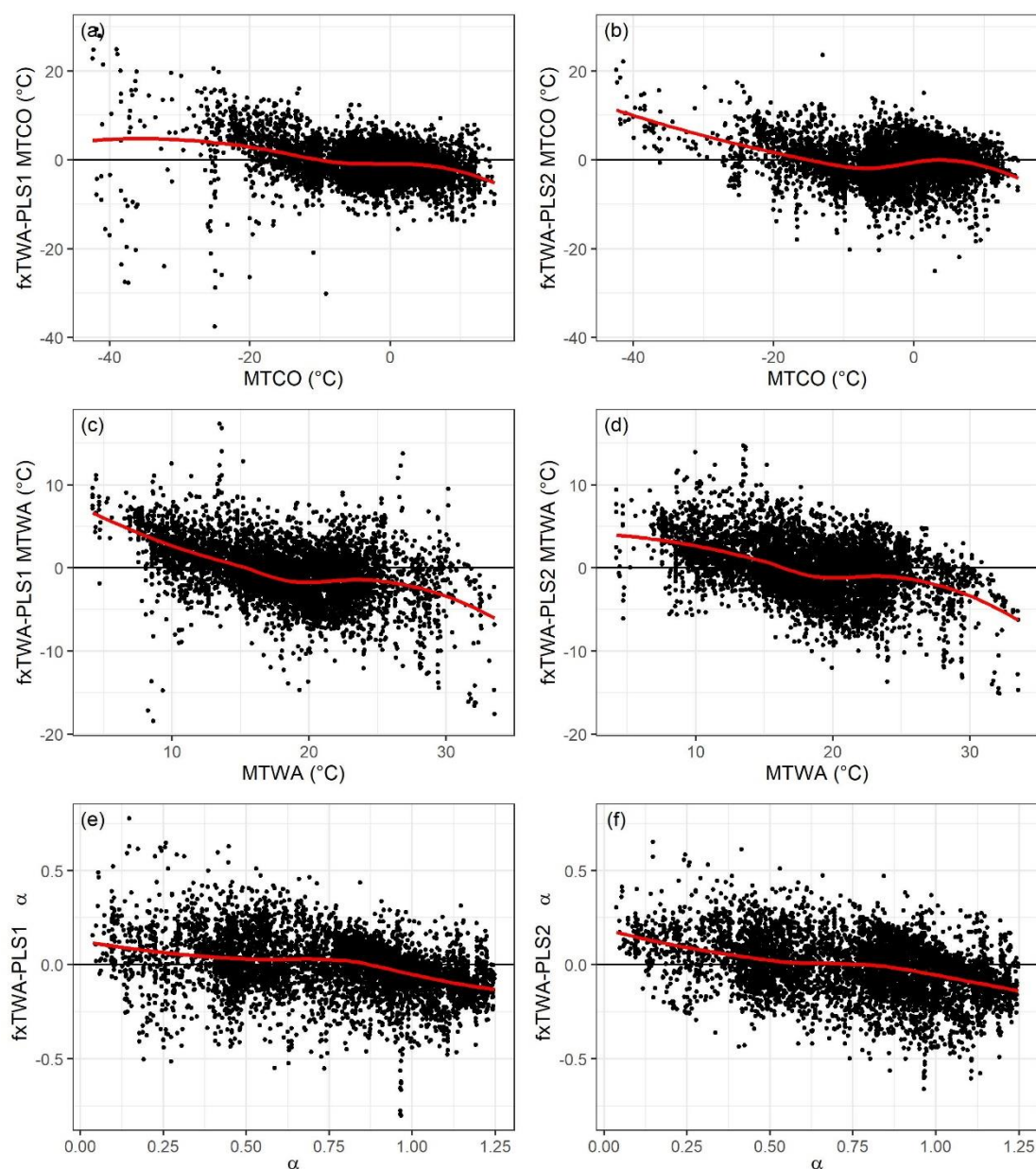
1042

1043 Figure A1. Training results using the last significant number of components. The left panel
 1044 shows the previous version (fxTWA-PLS1) and the right panel shows the modified version of
 1045 fxTWA-PLS (fxTWA-PLS2). The 1: 1 line is shown in black; the linear regression line is
 1046 shown in red, to show the degree of overall compression. The horizontal dashed lines indicate
 1047 the natural limit of α (0~1.26).
 1048



1049
 1050

1051 Figure A2. Residuals using the last significant number of components. The left panel shows
 1052 the previous version (fxTWA-PLS1) and the right panel shows the modified version (fxTWA-
 1053 PLS2) of fxTWA-PLS. The zero line is shown in black; the locally estimated scatterplot
 1054 smoothing is shown in red, to show the degree of local compression.
 1055



1056

1057 As shown in Table A1, Figure A1 and A2, the modified version is able to further reduce the
 1058 compression in MTCO and MTWA, and maximum bias in MTCO, MTWA and α . As shown
 1059 in Figure A1 and A2, there is less scatter and there are less α values beyond the natural limit.